Nanoscale Advances

Accepted Manuscript

This article can be cited before page numbers have been issued, to do this please use: Abdelfattah. Darwish, M. Morsy and M. Farouk, *Nanoscale Adv.*, 2026, DOI: 10.1039/D6NA00322B.

ROYAL SOCIETY OF CHEMISTRY

rsc.li/nanoscale-advances

View Article Online
DOI: 10.1039/D6NA00322B

Humidity-Dependent Dielectric and Electrical Behavior of Strontium Iron Vanadate Ceramics

Mohamed I. Farouk[1], Mohamed Morsy[2], Abdelfattah Darwish[3‡]

[1]*College of Engineering, Deanship of Scientific Research, Imam Mohammad Ibn Saud Islamic University (IMSIU), Riyadh 11432, Saudi Arabia.*
[2]*Nanotechnology Research Centre (NTRC), The British University in Egypt (BUE), Suez Desert Road, El-Sherouk City, Cairo 11837, Egypt.*
[3]*Microwave Physics and Dielectrics Department, Physics Research Institute, National Research Centre (NRC), 33 El-Bohouth St., Dokki, Giza, 12622, Egypt.*

Abstract:

Metal-oxide ceramics with perovskite-related structures offer tunable properties for sensing applications. The strontium iron vanadate ceramic system remains underexplored for humidity sensing despite theoretical interest in Sr_2FeVO_6-type compositions. This study presents sol-gel synthesis of strontium iron vanadate ceramic at 900°C and its characterization as an impedance-type humidity sensor. XRD revealed a multi-phase composition with a perovskite-related Ia-3d superstructure (a = 10.040 Å, 20 superstructure reflections systematically absent in Pm-3m) and Sr-vanadate phases. FTIR confirmed a hydrophilic metal-oxygen framework with BO_6 octahedral vibrations characteristic of perovskite-related structures. SEM showed ~1.6 μm grains with inter-particle porosity; DLS showed ~460 nm agglomerates. Zeta potential was −15 mV, indicating surface hydroxylation. Impedance spectroscopy (50 Hz–5 MHz, 11–97% RH) demonstrated 621%/%RH sensitivity at 50 Hz with two clearly separated conduction regimes: localized hopping mechanisms dominating at low RH and long-range proton transport occurring through continuous water pathways at elevated RH. The dielectric permittivity increased to approximately 10^6–10^7 at low frequencies, accompanied by a more conduction-related loss behavior at higher humidity, while the AC conductivity rose by nearly four orders of magnitude. This work reports humidity sensing properties of sol-gel-derived strontium iron vanadate ceramic with perovskite-related contributions and provides mechanistic insight into two-stage conduction behavior.

Keywords: strontium iron vanadate ceramic, perovskite-related structure, humidity sensor, impedance spectroscopy, sol-gel synthesis.

View Article Online
DOI: 10.1039/D6NA00322B

‡Corresponding author: Abdelfattah Darwish: abdelfatah.nrc@gmail.com.

Introduction

Double perovskites of the general formula $A_2BB'O_6$ have attracted sustained interest as a versatile family of functional oxide materials, owing to their tunable structural, electronic, magnetic, and dielectric properties arising from the ordered arrangement of two distinct transition metal cations on the B-site [1,2]. The mixed metal-oxygen surface terminations characteristic of double perovskite oxides are associated with surface hydroxylation and hydrophilic character favorable for water molecule interaction, properties relevant to impedance-type humidity sensing [3–6]. Sol-gel synthesis has proven particularly effective for producing high-purity Sr-based double perovskites at moderate sintering temperatures, enabling precise stoichiometric control and homogeneous cation distribution [7–10]. Despite the compositional flexibility and ordered cation sublattices of double perovskites, their potential as humidity sensing materials remains largely underexplored, with most impedance-type humidity sensors reported to date based on simple metal oxides or single perovskite compositions [3,4,11,12].

Among double perovskite compositions, the A_2FeVO_6 family has attracted theoretical interest following the prediction by Chen and Millis [13] that compositions with A = Ba, Sr, and Pb represent a new class of Mott multiferroics with promising photovoltaic and multifunctional properties. Subsequent experimental work confirmed the formation of Ba_2FeVO_6 by sol-gel synthesis [14], and Mg_2FeVO_6 by solid state reaction [15], establishing proof-of-concept for the A_2FeVO_6 family. Sr^{2+} ionic radius sits between that of both Ba^{2+} and Mg^{2+}. The Sr analogue Sr_2FeVO_6 represents a particularly attractive target, the smaller ionic radius of Sr^{2+} relative to Ba^{2+} yields a Goldschmidt tolerance factor within the cubic stability range, predicting cubic symmetry for the double perovskite structure favorable for isotropic grain boundary formation and uniform water vapor access across grain surfaces. The significant difference in ionic radius and charge between Fe^{3+} and V^{5+} B-site cations is expected to favor long-range B-site ordering in the synthesized material, generating heterogeneous Fe–O and V–O surface terminations expected to promote surface hydroxylation favorable for water molecule adsorption. The hydrophilic character of Sr-based perovskite oxides further supports moisture uptake across the full humidity range. To the best of our knowledge, Sr_2FeVO_6 has not been reported as a humidity sensing material.

View Article Online
DOI: 10.1039/D6NA00322B

The mechanistic understanding of humidity sensing in perovskite oxide materials, particularly the nature of the conduction transition that governs the impedance response across the full humidity range, remains incompletely characterized for double perovskite compositions [5,16–18]. Impedance spectroscopy combined with electric modulus and dielectric analysis provides a powerful and systematic framework for identifying and separating the contributions of grain boundary and grain interior relaxation processes to the overall sensing response, enabling mechanistic insight beyond simple impedance-versus-humidity characterization [16,19,20]. To the best of our knowledge, Sr_2FeVO_6 has not been reported as an impedance-type humidity sensing material.

In this work, Sr_2FeVO_6 was synthesized by sol-gel method at 900°C and characterized as an impedance-type humidity sensor across 11%–97% RH. Structural and microstructural characterization was performed using XRD, FTIR, SEM, DLS, and zeta potential measurements. Impedance spectroscopy combined with electric modulus and dielectric analysis was employed to identify grain boundary and grain interior relaxation contributions and elucidate the humidity-dependent conduction mechanism.

2. Experimental:

2.1 Materials

All reagents were of analytical grade and used without further purification. Ammonium metavanadate (NH_4VO_3) (obtained from SD fine-chem ltd), iron (III) nitrate nonahydrate ($Fe(NO_3)_3.9H_2O$) (obtained from Loba Chemie), while the Strontium Acetate Hemihydrate ($Sr(CH_3COO)_2).0.5H_2O$ was obtained from from Sigma Aldrich, and citric acid anhydrous ($(C_6H_8O_7)$ was purchased from (PanReac AppliChem). The glacial acetic acid (CH_3COOH) was obtained from ADWIC. Deionized water was used in all preparations.

2.2 Sol–Gel Synthesis of strontium iron vanadate ceramic.

The strontium iron vanadate has been prepared by the sol-gel method, using three precursor solutions prepared separately before mixing under controlled conditions. First, the strontium

View Article Online
DOI: 10.1039/D6NA00322B

acetate solution was obtained by dissolving 0.0165 mol of strontium acetate hemihydrate in 30 mL of deionized water and 10 mL of glacial acetic acid (3:1 v/v, water/acetic acid) at room temperature until complete dissolution. Second, 0.0165 mol of $Fe(NO_3)_3.9H_2O$ was dissolved in 20 mL of deionized water at room temperature, while 0.0165 mol of ammonium metavanadate was dissolved in deionized water at 80 °C due to its limited solubility at room temperature. The three precursor solutions were mixed thoroughly, keeping the molar ratio at 2:1:1 for Sr: V: Fe solutions. The solutions of iron nitrate and ammonium metavanadate were added to the strontium acetate solution and kept under stirring for another 4 hours at 80 °C. Citric acid with a molar ratio of 3:1 relative to the total metal ion content was added dropwise during the stirring process, maintaining the temperature at 80 °C until a viscous gel was formed, then dried overnight at 120 °C. The dried powder was ground and sintered in air for 6 hours at 900°C and left to cool naturally to room temperature. The schematic representation of the synthesis procedure is presented in **Figure 1**.

2.3 Measurement devices

XRD patterns were obtained using a Malvern Panalytical Empyrean 3 diffractometer (CuKα wavelength 1.5406 Å). The SEM instrument (Quattro S, Thermo Scientific), operated at 20 kV, was used to obtain the morphological features. The Malvern Panalytical Zetasizer was used for dynamic light scattering (DLS) size distribution and zeta potential measurements. The dielectric conditions were understood by engaging over a range of frequencies (50 to 5 MHz).

2.4 Sensor fabrication and testing

The humidity sensor was fabricated using sensing material that has been deposited on the surface of the fluorinated tine oxide substrate (FTO). The sensing material was grounded well in an agate mortar, with a few drops of de-ionized water to form a homogeneous paste. The paste was spread over FTO using the doctor-blade/cast method onto the FTO substrate, then dried at 150°C for 8 hours. The fabricated thick film has been used for both electrical measurements and sensor evaluation. The measured electrical parameters are total impedance magnitude |Z| (Ω), phase angle θ (degrees), real impedance component Z′ (Ω), and imaginary impedance component Z″ (Ω). From these primary measurements, the other electrical parameters were calculated. The fabricated sensor was conditioned at 11% RH and 97% RH for 24 hours, then measured at different RH levels by applying 1volt ac signal across frequencies from 50 Hz to 5 MHz. The required RH level was kept

View Article Online
DOI: 10.1039/D6NA00322B

stable inside a sealed conical flask containing saturated salt solutions. The saturated salt solutions were obtained by dissolving analytical grade salts in distilled water. Controlled humidity environments were generated inside sealed conical flasks using saturated salt solutions prepared following ASTM E104-02. Lithium chloride, potassium acetate, potassium carbonate, sodium chloride, potassium chloride, and potassium sulfate were used to produce 11%, 23%, 43%, 75%, 84%, and 97% RH respectively. The fabricated sensor was attached with two alligator clips and suspended freely over a saturated salt solution and allowed to stabilize for 30 minutes. Once the impedance value of the sensor remained constant or fluctuated within 3%, the corresponding impedance value was recorded using the HIOKI-3532-50 LCR bridge. The represented data is the average of three measurements taken each one-minute interval at each RH level. The response and recovery times were estimated from repeatability curves. All tests were conducted at room temperature. A schematic diagram of the experimental setup is shown in **Figure 1C.**

View Article Online
DOI: 10.1039/D6NA00322B

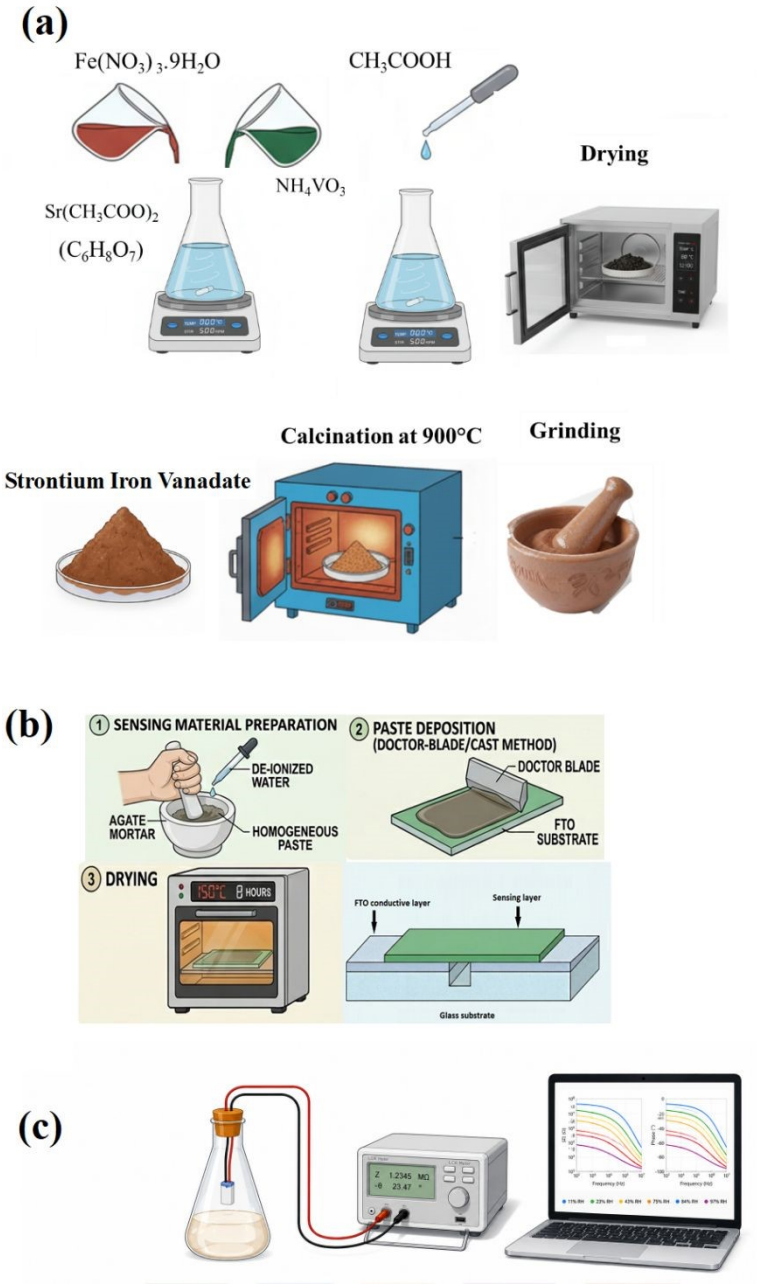

Fig.1: (a) Schematic diagram of the strontium iron vanadate ceramic preparation (b) Fabrication process of the humidity sensor: (1) preparation of a homogeneous paste by grinding the powder with de-ionized water, (2) deposition onto an FTO-coated glass substrate via doctor-blade casting, and (3) drying at 150 °C for 8 h; the inset shows the cross-sectional layered structure (c) Experimental setup for humidity sensing measurements showing the sensor suspended inside a sealed flask containing a saturated salt solution, connected to a HIOKI-3532-50 LCR meter for impedance characterization.

View Article Online
DOI: 10.1039/D6NA00322B

3. Results and discussion:

3.1 XRD Analysis

X-ray diffraction patterns over the 2θ range of 10° to 90° for the prepared strontium iron vanadate ceramics is presented in **Fig.2**. The XRD pattern shows sharp, well-defined peaks with no broad amorphous background, confirming that crystalline phases formed at 900°C. The XRD pattern shows 52 diffraction peaks in this range.

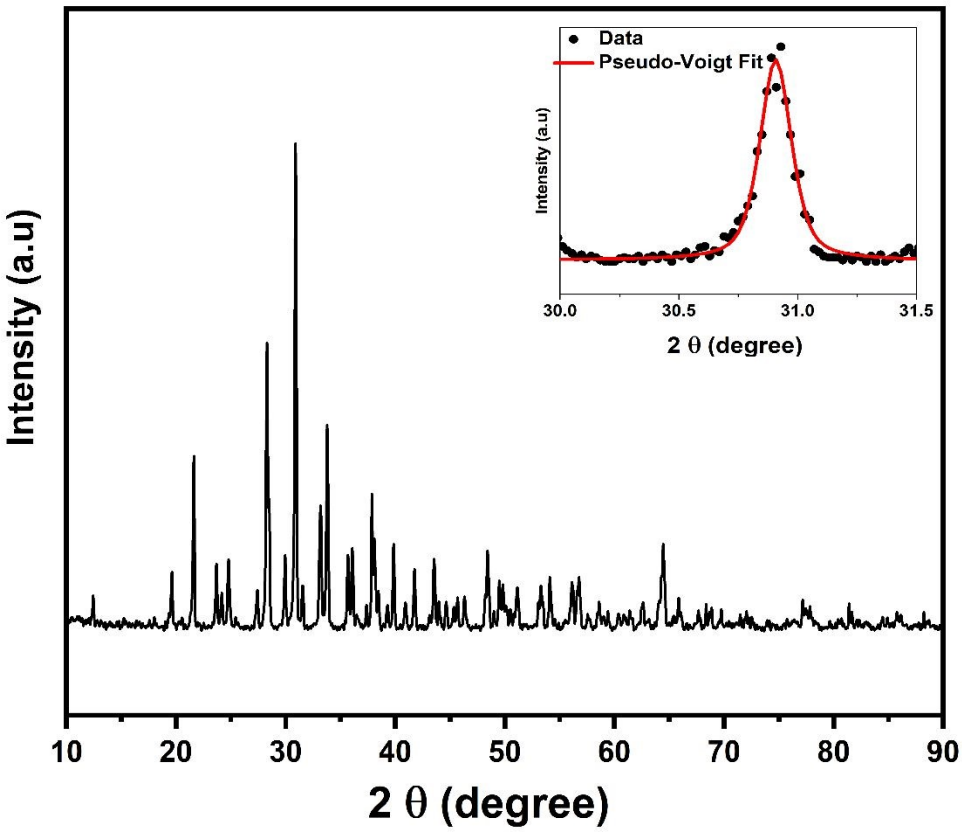

Fig. 2. XRD pattern of the strontium iron vanadate ceramic sintered at 900 °C. The inset represents the pseudo-Voigt function fitting of the (222) reflection at 2θ = 30.9°, (FWHM = 0.1586°, R^2 = 0.956) used for Scherrer crystallite size determination.

The pattern was indexed against a cubic double perovskite-related structure with space group Ia-3d (No. 230) and lattice parameter a = 10.040 ± 0.076 Å, obtained by least-squares refinement of 42 matched peaks. The 20 confirmed superstructure reflections (Table 1) violate the reflection conditions of Fm-3m but are permitted in Ia-3d, providing direct evidence for this space group assignment. Ia-3d has been identified among the phases present in the related compound

View Article Online
DOI: 10.1039/D6NA00322B

Mg_2FeVO_6 [6], indicating that this space group can also occur in A_2FeVO_6-type systems. Several reflections appear as closely spaced pairs with separations of 0.19–0.62°, substantially exceeding the expected Kα1/Kα2 splitting. Analysis of the doublet components yields two domain populations with lattice parameters a_1 = 10.048 Å and a_2 = 9.935 Å (Δa = 1.13%), consistent with microstructural inhomogeneity in sol-gel-derived ceramics. Both components index to the same hkl within geometric tolerance, supporting assignment to a single cubic phase with lattice parameter variation between domains. The 42 indexed peaks show no reflections violating Ia-3d extinction conditions, and no evidence of lower symmetry was observed.

The indexing was performed geometrically using observed d-spacings matched to calculated positions from the cubic Ia-3d cell (a = 10.040 Å). Deviations within ±2% are consistent with the precision of geometric indexing. The subcell relation gives a_{sub}= a/2 = 5.020 ± 0.038 Å, consistent with $A_2BB'O_6$ double perovskite stoichiometry. A total of 42 of 52 peaks (81% by count, ~60% by intensity) were indexed to this phase. Of the remaining 10 peaks, 6 are assigned to Sr-vanadate secondary phases and 4 remain unassigned. Complete peak assignments for all 52 reflections, including the 6 secondary phase peaks and 4 unassigned peaks, are provided in **Table S1 (Supplementary Material)**. Of the 26 confirmed superstructure ordering reflections, 20 carry relative intensities of I% ≥ 5% and are listed in **Table 1**. The remaining 6 ordering reflections with I% below 5% are included in Table S1.

The dominant peak at 2θ = 30.915° (d = 2.893 Å) is indexed as the (222) reflection. The Goldschmidt tolerance factor (t) was calculated using Shannon ionic radii [7] with appropriate coordination numbers and oxidation states: Sr^{2+} (CN = 12, r = 1.44 Å), Fe^{3+} high-spin (CN = 6, r = 0.645 Å), V^{5+} (CN = 6, r = 0.540 Å), and O^{2-} (CN = 6, r = 1.40 Å).

$$t = \frac{r_{Sr} + r_O}{\sqrt{2}\left(\frac{r_V + r_{Fe}}{2} + r_O\right)} = 1.008$$

The calculated t is consistent with cubic symmetry in double perovskites [2,21]. The cubic symmetry identified for the perovskite-related component (t = 1.008) contrasts with the hexagonal R-3c structure reported for the Ba-based iron vanadate double perovskite Ba_2FeVO_6 [14], where the larger Ba^{2+} ionic radius (r = 1.61 Å, CN = 12) yields t = 1.078, placing it in the hexagonal stability field (t > 1.05). The structural divergence between the Ba and Sr analogues is consistent

View Article Online
DOI: 10.1039/D6NA00322B

with tolerance factor predictions and reflects the systematic effect of A-site cation size on symmetry selection in A_2FeVO_6 double perovskites.

In an $A_2BB'O_6$ double perovskite, B-site cation ordering creates a supercell doubled relative to the simple perovskite subcell. This generates superstructure reflections at positions that are forbidden in the disordered simple perovskite [9]. Peaks with all-even Miller indices are fundamental, and are present in both simple and double perovskites. Peaks with odd or mixed indices are superstructure reflections only, strictly forbidden in disordered simple perovskite and present only when B-site ordering exists. The present pattern contains 26 confirmed superstructure ordering peaks across the full 10–90° range. The 20 most significant (I% ≥ 5) are listed in **Table 1.** The 2nd strongest peak in the entire pattern (I% = 58.1 at 2θ = 28.310°) and the 4th strongest peak (I% = 34.5 at 2θ = 21.636°) are both superstructure ordering reflections. These peaks are systematically absent in disordered simple perovskite (Pm-3m); their presence at significant relative intensities indicates B-site cation ordering in the perovskite-related component.

The effect of A-site cation substitution on symmetry selection across the A_2FeVO_6 family provides important structural context for the present results. Three A-site cations have been reported in this system: Ba^{2+}, Sr^{2+}, and Mg^{2+}. Their Goldschmidt tolerance factors differ substantially, and the structural outcomes reflect this difference directly.

Ba^{2+} carries the largest ionic radius in this series (r = 1.61 Å, CN = 12), giving t = 1.078 for Ba_2FeVO_6 [14]. This value exceeds the cubic stability threshold and places Ba_2FeVO_6 in the hexagonal stability field. Pei et al. [14] confirm that Ba_2FeVO_6 prepared by solid-state synthesis crystallizes in hexagonal R-3c, with characteristic reflections at 2θ = 27.52° and 30.96° and lattice parameters a = 10.08–10.14 Å and c = 24.38–24.45 Å. Bhran et al. [22], using a sol-gel citric acid complexation route analogous to the present work, confirm the same hexagonal R-3c structure for Ba_2FeVO_6 at 900°C, with a crystallite size of 44.7 nm. At lower sintering temperatures, Bhran et al. [22] document $BaCO_3$, $Ba_2V_2O_7$, and Fe_2O_3 as intermediate impurity phases that reduce progressively with increasing temperature, reaching maximum phase purity at 900°C.

At the other end of the size range, Mg^{2+} produces a markedly different structural outcome. Sahu et al. [15] report that Mg_2FeVO_6 prepared by solid-state synthesis at 1100°C yields a three-phase mixture with no clean double perovskite structure, as described above.

View Article Online
DOI: 10.1039/D6NA00322B

Sr^{2+} sits between Ba^{2+} and Mg^{2+} in ionic radius (r = 1.44 Å, CN = 12), giving t = 1.008 for the present Sr_2FeVO_6 material. This value falls within the cubic stability range. Consistent with this prediction, the present XRD pattern shows none of the hexagonal R-3c reflections characteristic of Ba_2FeVO_6 at 2θ = 27.52° and 30.96°, and none of the orthorhombic or garnet-range phases reported for Mg_2FeVO_6. Instead, the pattern shows a single cubic Ia-3d phase with a = 10.040 Å, with 20 confirmed superstructure reflections above the 5% intensity threshold providing direct evidence for B-site ordering. The impurity profile is limited to Sr-vanadate secondary phases with no carbonate formation observed.

Across the A_2FeVO_6 family, A-site cation size is therefore the dominant factor controlling symmetry selection. Reducing the A-site from Ba^{2+} (t = 1.078) drives the structure out of the hexagonal R-3c field. Sr^{2+} (t = 1.008) uniquely stabilizes the cubic Ia-3d double perovskite with confirmed B-site ordering. Mg^{2+} at a lower tolerance factor produces a mixed-phase outcome under the reported solid-state synthesis conditions.

Table 1. Superstructure ordering peaks (I% > 5), forbidden in disordered simple perovskite (Pm-3m). ★ = among the strongest peaks in the pattern. $d_{indexed}$ calculated from cubic Ia-3d, a = 10.040 Å. 𝕏 = marginally exceeds ±2.0% tolerance.

$2\theta_{obs}$ (°)	d_{obs} (Å)	I%	hkl	$d_{indexed}$ (Å)	Δ%	Note
12.452	7.109	8.7	(110)	7.092	+0.2	ordering
21.636	4.108	34.5	(211)	4.094	+0.3	ordering
28.310	3.153	58.1	(310)	3.171	−0.6	ordering ★
28.502	3.132	25.8	(310)	3.171	−1.2	ordering
33.188	2.699	26.4	(321)	2.680	+0.7	ordering
33.787	2.653	53.9	(321)	2.680	−1.0	ordering ★
37.385	2.406	5.27	(330)	2.364	+1.8	Ordering 𝕏
37.865	2.376	31.2	(330)	2.364	+0.5	ordering
38.121	2.361	18.8	(330)	2.364	−0.1	ordering
38.471	2.340	7.28	(330)	2.364	−1.0	ordering

View Article Online
DOI: 10.1039/D6NA00322B

41.766	2.163	12.3	(332)	2.138	+1.2	ordering
45.714	1.985	5.60	(431)	1.967	+0.9	ordering
46.326	1.960	6.39	(431)	1.967	−0.3	ordering
49.469	1.843	8.6	(521)	1.831	+0.7	ordering
53.380	1.716	5.88	(433)	1.720	−0.2	ordering
56.136	1.638	10.2	(532)	1.627	+0.7	ordering
56.752	1.622	10.8	(532)	1.627	−0.3	ordering
62.558	1.485	5.24	(631)	1.479	+0.4	ordering
68.365	1.371	15.4	(552)	1.365	+0.5	ordering
77.207	1.236	5.9	(554)	1.235	+0.1	ordering

Of the 52 peaks identified in the full pattern, 42 were indexed to the cubic Ia-3d perovskite-related phase, 6 were assigned to Sr-vanadate phases, and 4 remain unassigned. A total of 37 peaks with relative intensity I% ≥ 5 were identified in the 10–90° range. Of these, 29 peaks were indexed to the cubic Ia-3d phase (20 superstructure ordering reflections and 9 fundamental reflections). Six peaks were assigned to Sr-vanadate contributions and two peaks remain unindexed. Full peak indexing data for all 52 peaks are provided in **Table S1** (Supplementary Material).

Six peaks in the pattern could not be indexed to the perovskite-related phase. These peaks were screened against known Sr–V–O and Sr–Fe–O reference phases from the ICDD PDF and COD databases. $Sr_{10}V_6O_{25}$ (PDF 00-052-1578, hexagonal P63/m, a = 10.063 Å, c = 7.415 Å) provides tentative matches for peaks at 2θ = 23.69° (d = 3.755 Å, deviation 1.27%, hkl 002), 27.42° (d = 3.253 Å, deviation 1.24%, hkl 210), 29.95° (d = 2.984 Å, deviation 0.03%, hkl 112), 31.59° (d = 2.833 Å, deviation 0.32%, hkl 202), 39.30° (d = 2.293 Å, deviation 0.22%, hkl 311), and 48.44° (d = 1.879 Å, deviation 0.05%, hkl 402). Sr_2VO_4 (PDF 01-085-2430, orthorhombic Pna21, a = 14.088 Å, b = 5.809 Å, c = 10.110 Å) provides tentative matches for peaks at 2θ = 19.63° (d = 4.522 Å, deviation 1.1%, hkl 211), 24.19° (d = 3.680 Å, deviation 0.03%, hkl 112), and 24.78° (d = 3.593 Å, deviation 1.7%, hkl 311). The peak at 2θ = 5.172° (d = 17.088 Å, I% = 3.09) does not match any reference phase screened and is attributed to instrumental background scatter at very low angles. No single reference phase accounts for all minor phase peaks simultaneously, indicating a multi-component Sr–vanadate contribution. These minor phase contributions are

View Article Online
DOI: 10.1039/D6NA00322B

present in insufficient quantity to affect the dominant phase identification or the functional properties reported in this work. The absence of detectable Fe-containing secondary phases in the pattern is consistent with incorporation of Fe^{3+} into the perovskite-related Ia-3d phase, supported by the presence of 20 superstructure reflections at significant relative intensities that are characteristic of B-site cation ordering between Fe^{3+} and V^{5+}. The possibility that Fe-containing minor phases are present below the detection threshold of the measurement cannot be completely excluded.

Crystallite size was estimated using the Scherrer equation applied to the isolated (222) reflection at $2\theta = 30.908°$, fitted with a pseudo-Voigt function (FWHM (β) = 0.1586°, $R^2 = 0.956$, **Fig. 2** inset): $D = K\lambda / (\beta \cos\theta) = 51.4$ nm, where K = 0.89 (Scherrer shape factor), $\lambda = 1.5406$ Å. The strong (310) reflection at 28.310° was excluded due to overlap with a satellite peak at 28.502°. Williamson-Hall analysis was not attempted due to extensive peak overlap throughout the pattern.

The structural characteristics of the present material show synthesis dependence when compared with the solid-state route reported by Sahu et al. [15] for Mg_2FeVO_6. Their calcination at 1050°C and sintering at 1100°C produced a three-phase mixture: cubic P4,32 (a = 8.38 Å, 31.65%), cubic Ia-3d (a = 12.43 Å, 43.92%), and orthorhombic Pnma (a = 9.791, b = 3.687, c = 12.727 Å, 24.43%). The dominant Ia-3d phase reported by Sahu et al. carries a lattice parameter of 12.43 Å, which exceeds the typical $A_2BB'O_6$ double perovskite range of approximately 10 Å. The present sol-gel synthesis at 900°C yields a single Ia-3d phase with a = 10.040 Å, consistent with established double perovskite-related stoichiometry, with no orthorhombic or garnet-range phases observed. Crystallite sizes differ between the two studies: Sahu et al. report 38.9 nm by Scherrer analysis from their multiphase mixture, compared with 51.4 nm in the present work. Direct comparison is limited by the differences in A-site cation, phase composition, and synthesis route between the two studies.

The present study employs geometric indexing and superstructure reflection analysis to establish phase identity and cell metric. The identification of 20 superstructure reflections that are systematically absent in disordered Pm-3m but permitted in Ia-3d provides crystallographic evidence for B-site ordering, consistent with features related to Sr_2FeVO_6-type double perovskite ordering. Detailed structural refinement is beyond the scope of the present work, which focuses on the synthesis, characterization, and humidity sensing performance of this material.

View Article Online
DOI: 10.1039/D6NA00322B

3.2 FTIR Analysis.

Complementary structural information was obtained from FTIR spectroscopy presented in Fig. 3. The FTIR spectrum of strontium iron vanadate ceramic, recorded in the range 4000–400 cm^{-1}, reveals characteristic vibrational features consistent with perovskite-related and vanadate contributions. The broad absorption band at 3383 cm^{-1} and the bending mode at 1630 cm^{-1} are attributed to O–H stretching and H–O–H bending vibrations of adsorbed water molecules, respectively, indicating hydrophilic surface character, which is a prerequisite for humidity sensing activity. A weak band at 1449 cm^{-1} is attributed to trace carbonate species, arising from surface adsorption of atmospheric CO_2; its weakness is consistent with effective decomposition of carbonate intermediates during sintering at 900°C.

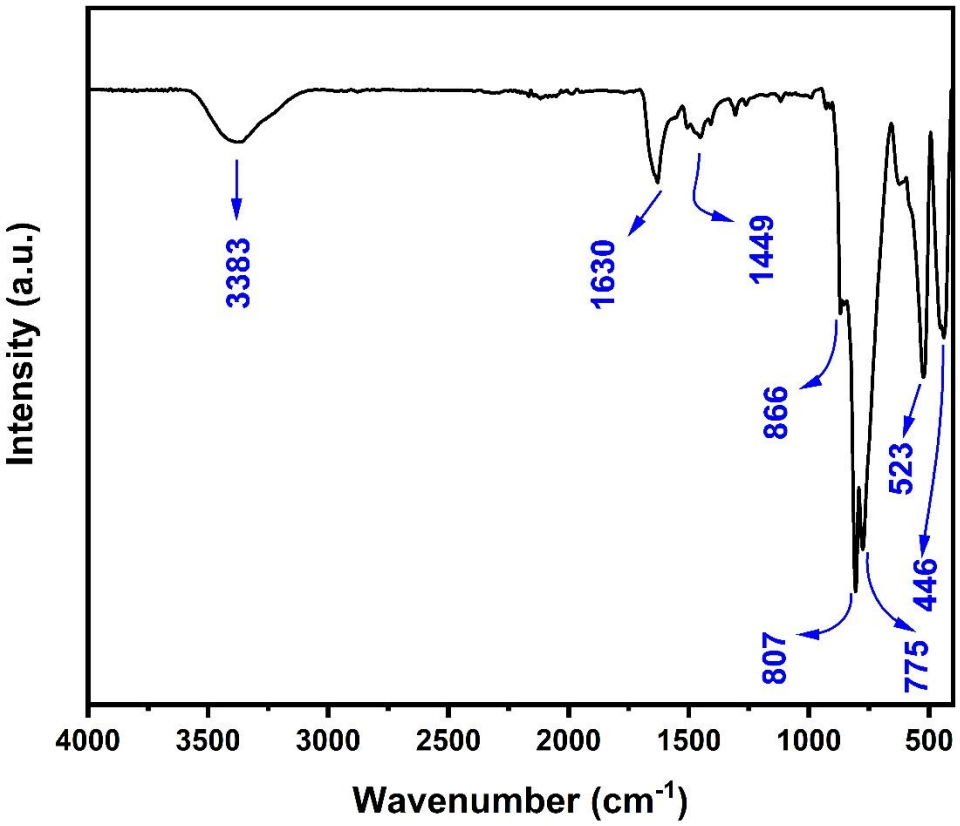

Fig. 3. FTIR spectrum of strontium iron vanadate ceramic sintered at 900°C recorded in the range 4000–400 cm^{-1}. Assigned vibrational bands are indicated by arrows. Assigned

View Article Online
DOI: 10.1039/D6NA00322B

vibrational bands consistent with BO_6 octahedral framework vibrations characteristic of perovskite-related structures and hydrophilic surface character from adsorbed water.

The metal–oxygen stretching region below 900 cm^{-1} provides confirmation of the BO_6 octahedral framework vibrations characteristic of perovskite-related structures. The dominant band at ~807 cm^{-1} is attributed to the collective symmetric stretching of the BO_6 octahedral framework, representing the primary metal–oxygen vibrational mode of the perovskite lattice. Two additional bands are observed at ~866 cm^{-1} and ~775 cm^{-1}, are tentatively assigned to metal–oxygen stretching vibrations in different octahedral environments, reflecting B-site cation disorder consistent with multi-phase composition. The higher frequency band is consistent with higher oxidation state cations (shorter bond length, higher force constant) compared to the lower frequency band [23]. The band at ~523 cm^{-1} is attributed to antisymmetric bending vibrations of BO_6 octahedra [24,25], and the band at ~446 cm^{-1} corresponds to lattice vibrational modes [1,24].

The observation of multiple resolved bands in the metal–oxygen stretching region supports the formation of a perovskite-related framework with B-site cation environments, consistent with XRD results showing perovskite-related and vanadate contributions. The FTIR and XRD data together indicate structural features related to Sr_2FeVO_6-type ordering within a multi-phase metal-oxide system. These structural and hydrophilic surface characteristics provide the basis for the humidity sensing behavior reported in **Section 3.6**.

3.3 Surface Morphology

Fig. 4 shows SEM images of strontium iron vanadate ceramic at two magnifications. The left image is at 6,000× with a scale bar of 10 μm. The right image is at 25,000× with a scale bar of 3 μm. The micrographs reveal a granular microstructure composed of well-defined, polyhedral grains with an average size of approximately 1.6 μm (inset, **Fig. 4a**). The particle size distribution, determined by manual measurement of 50 grains using ImageJ software, shows a broad distribution with a shoulder at ~2.3 μm. The majority of grains fall within the 1.0–2.0 μm range, with few particles exceeding 2.5 μm. At higher magnification (**Fig. 4b**), individual grains exhibit faceted surfaces and well-formed edges. The grains appear reasonably well-packed, with inter-particle porosity visible between grain clusters, suggesting partial densification during sintering at

View Article Online
DOI: 10.1039/D6NA00322B

900°C. The granular morphology observed is consistent with perovskite-related contributions identified by XRD. The average grain size of ~1.6 µm observed by SEM substantially exceeds the crystallite size of 51.4 nm determined by Scherrer analysis, indicating that each observed grain comprises multiple nanocrystallite domains. This hierarchical structure (nanocrystallite aggregates forming micron-scale grains) is typical of sol-gel derived strontium iron vanadate ceramics and provides the high surface area and grain boundary density favorable for humidity sensing applications.

The surface morphology of the as-deposited Sr_2FeVO_6 thick film on FTO is shown in **Fig. 5.** At low magnification (1000×), the film exhibits a rough, granular surface with visible inter-agglomerate voids. At higher magnification (5000×), polyhedral grains consistent with the parent powder are resolved, separated by inter-particle gaps. These morphological features provide a microstructural basis for the humidity-dependent impedance and dielectric behavior presented in the following sections.

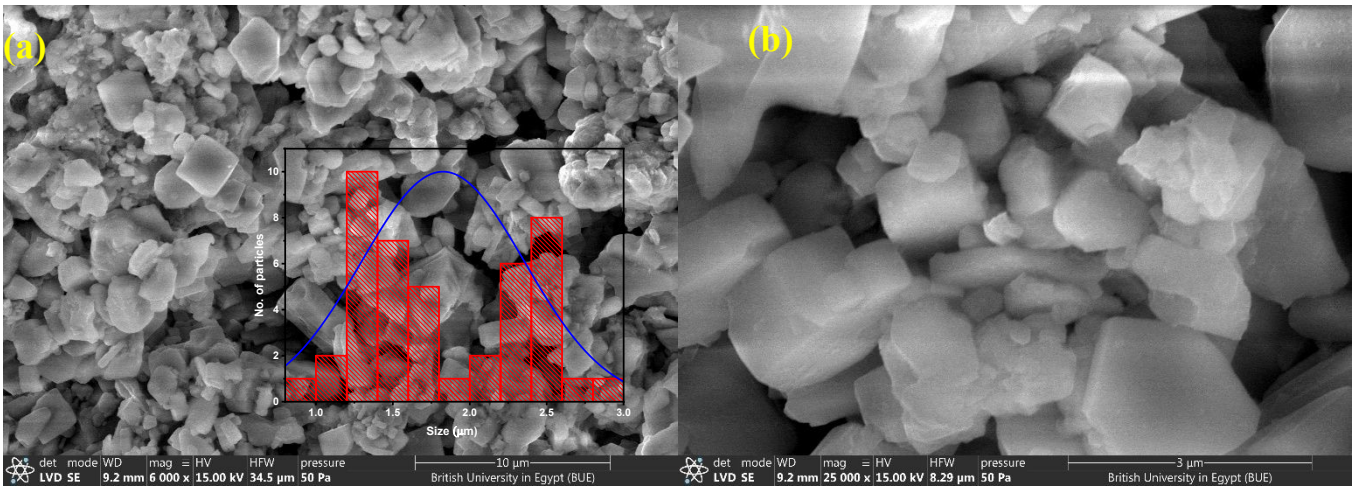

Fig. 4. SEM micrographs of Sr_2FeVO_6 at different magnifications; (a) 6,000× magnification with inset showing particle size distribution (n = 50), and (b) 25,000× magnification showing detailed grain morphology.

View Article Online
DOI: 10.1039/D6NA00322B

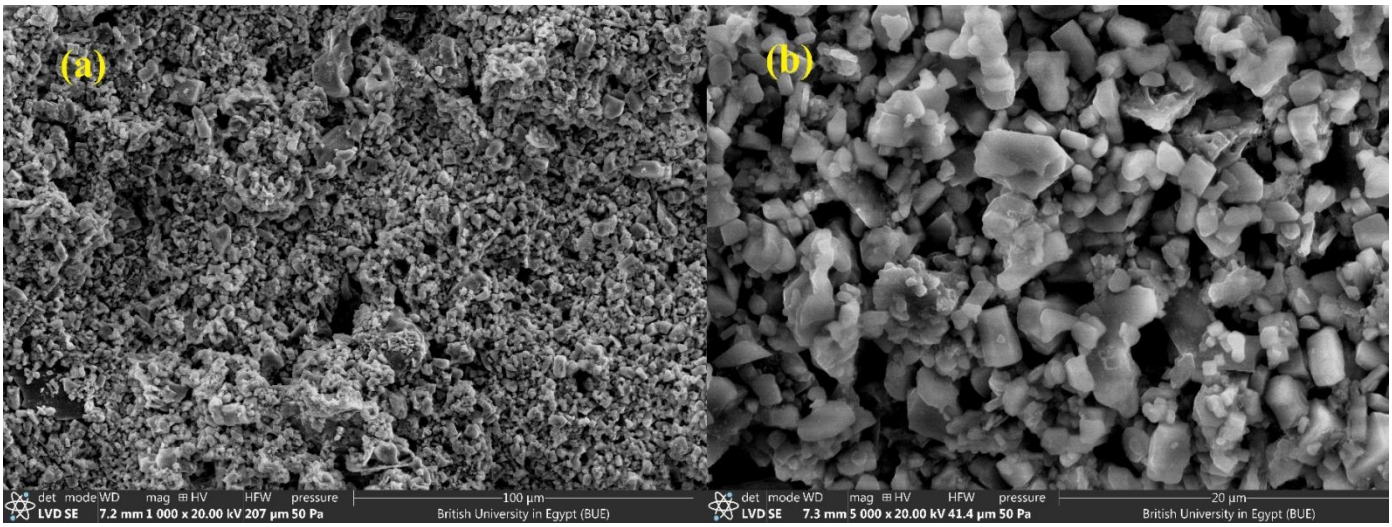

Fig. 5. SEM micrographs of the as-deposited Sr_2FeVO_6 thick film on FTO: (a) 1000× magnification (scale bar 100 µm) showing the overall granular surface with inter-agglomerate porosity, and (b) 5000× magnification (scale bar 20 µm) revealing individual polyhedral grains and inter-particle voids.

3.4 Particle size distribution by DLS

The hydrodynamic particle size distribution of strontium iron vanadate ceramic was measured by dynamic light scattering (DLS) following dispersion in deionized water with 10 minutes of ultrasonication. The intensity-weighted size distribution is shown in **Fig. 5**. The DLS results show two peaks; a main peak at ~360 nm, reflecting the majority of the scattering intensity, and a minor small peak at ~5000 nm. The main peak (~360 nm) comes from particle agglomerates in water. This is larger than the crystallite size from XRD (51.4 nm) but smaller than the grain size from SEM (~1600 nm). This means the 51 nm crystallites group together in water to form ~460 nm clusters. The sonication broke some of the large grains apart, but not all the way down to single crystallites. The dominant peak is attributed to partially disaggregated particle clusters in suspension. The minor peak at ~5000 nm is consistent with residual large agglomerates that were not fully dispersed under the applied sonication conditions, corresponding to the larger grain clusters observed in the SEM micrographs [12].

View Article Online
DOI: 10.1039/D6NA00322B

The poly dispersity index (PdI) of 0.478 confirms a broad particle size distribution, consistent with the grain size range of 1.0–2.5 µm observed by SEM. It should be noted that DLS measures hydrodynamic diameter in suspension, which reflects both particle size and surface hydration layer thickness, and is therefore not directly comparable to solid-state measurements from XRD or SEM. The tendency toward agglomeration indicated by the PdI and the minor large-agglomerate peak is consistent with the inter-particle porosity observed by SEM, which contributes to the accessible surface area available for water molecule adsorption.

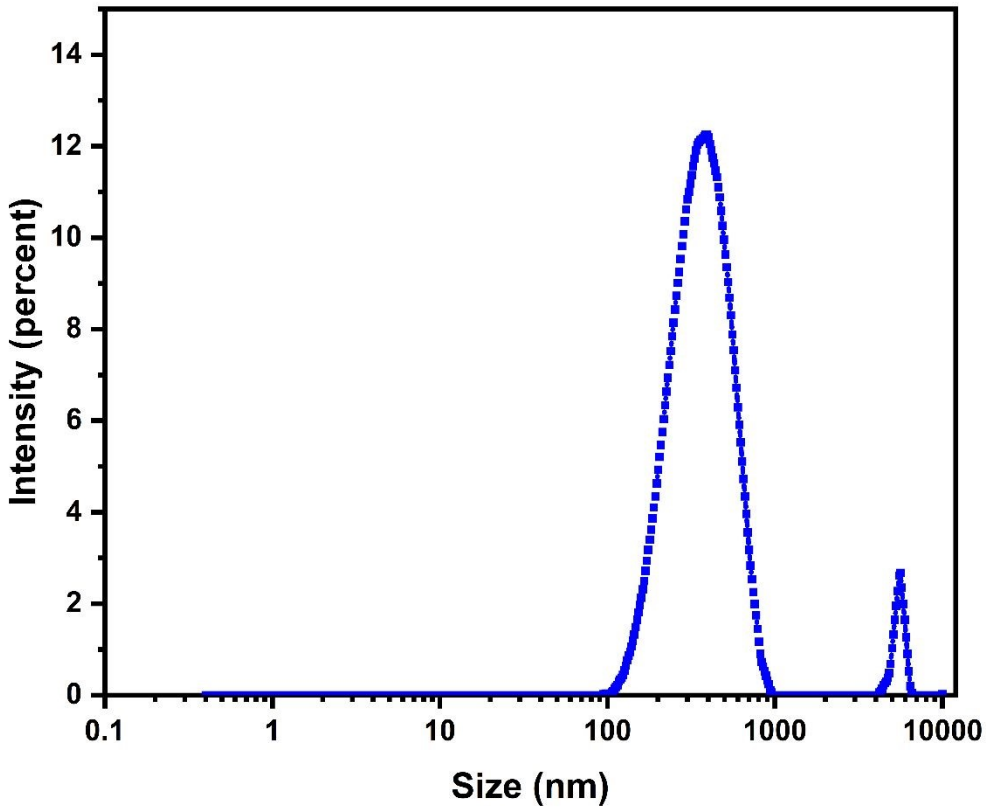

Fig. 6. Intensity-weighted hydrodynamic particle size distribution of strontium iron vanadate ceramic measured by DLS following dispersion in deionized water. The dominant peak at ~360 nm corresponds to partially disaggregated particle clusters, and the minor peak at ~5000 nm corresponds to residual large agglomerates.

View Article Online
DOI: 10.1039/D6NA00322B

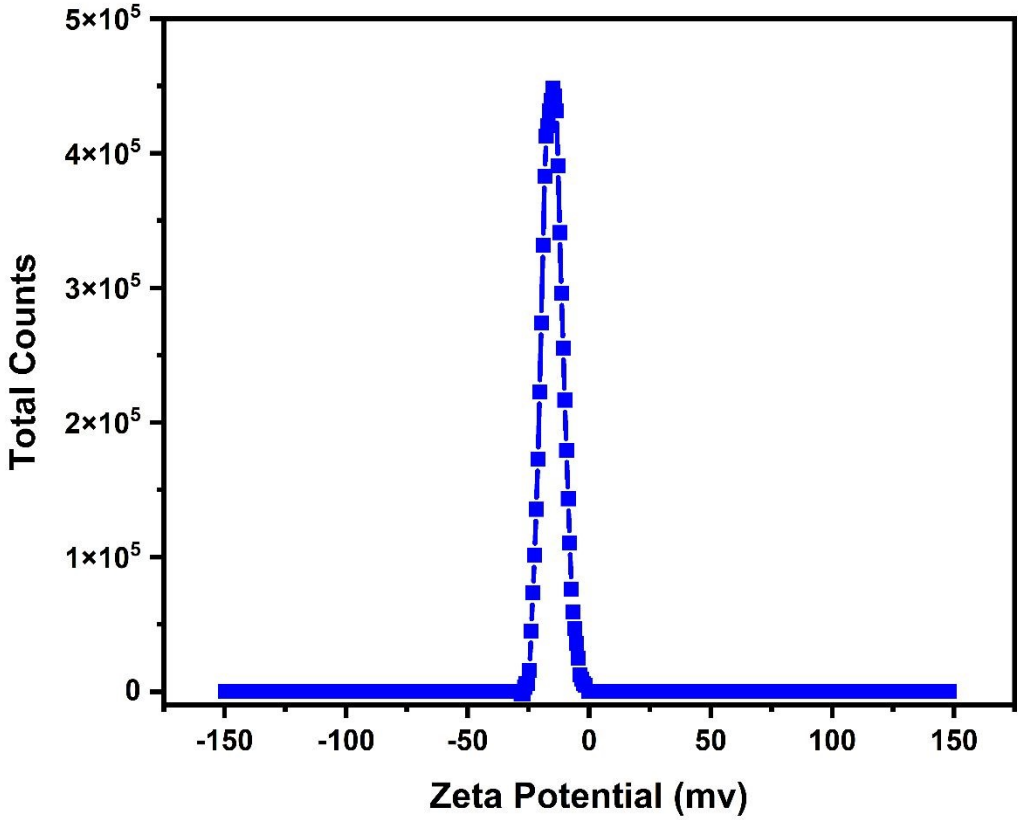

Fig. 7. Zeta potential distribution of strontium iron vanadate ceramic in aqueous suspension, showing a single peak at approximately -15 mV indicating negatively charged surfaces from hydroxyl group termination.

3.5 Zeta Potential Analysis

Zeta potential is a critical tool for understanding the interaction between the materials and water molecules in humidity sensing applications. The surface charge characteristics of strontium iron vanadate ceramic were evaluated by zeta potential measurement in aqueous suspension (**Fig. 6**). The distribution exhibits a single, narrow peak centered at approximately -15 mV, indicating a negatively charged surface. A zeta potential of -15 mV falls below the conventional stability threshold of ±30 mV, indicating a tendency toward agglomeration in suspension. This is consistent with the broad PdI (0.478) and large-agglomerate peak observed in the DLS measurement. The negative zeta potential arises from surface hydroxylation of the strontium iron vanadate ceramic in an aqueous environment, where exposed metal-oxygen sites react with water to form hydroxyl (–OH) groups. The moderate negative surface charge indicates sufficient surface activity for

View Article Online
DOI: 10.1039/D6NA00322B

moisture uptake. The unimodal zeta potential distribution suggests a relatively homogeneous surface charge across the particle population, which supports consistent sensing response. The negative surface charge is expected to facilitate water molecule adsorption through electrostatic interaction with dipolar water molecules, complementing the hydrophilic character confirmed by FTIR and providing a mechanistic basis for the humidity sensing performance discussed in **Section 3.6**.

3.6.1 Humidity sensing performance

The impedance type humidity sensors are dependent on applied AC frequency, so the effect of applied frequency on the response was studied, as shown in **Fig. 7**. It was noted that at all testing frequencies, the impedance decreases as the RH level increases from 11% up to 97%. The impedance curves are influenced by the applied testing frequency, as the frequency increases, the total change in impedance decreases. This is a well-known behavior for all humidity sensors, where the polarizability of the adsorbed water molecules is affected by the applied frequency [5,12]. Water molecules are polar in nature with a total dipole of 1.85 Debye [18]. At low applied frequency the water molecules have enough time to align themselves with the applied AC signal, while as the frequency increases, water molecules cannot flip fast enough to follow the field, hence the total impedance change at high frequency is less than that at low frequency. The optimum test frequency is the frequency at which the total impedance change is maximum, which was achieved at 50 Hz so for further evaluation of the humidity sensor, the frequency of the applied AC signal will be set at 50Hz. The change in impedance as a function of relative humidity at 50%RH is shown in **Fig. 7b**. The normalized sensitivity of the studied sensor has been calculated using the following equation [17]

$$Sn = \left(\frac{\frac{Z_{\max} - Z_{min}}{Z_{min}}}{\Delta RH} \right) * 100$$

Where Z_{max} and Z_{min} are the impedance at 97% and 11%RH respectively.

The normalized response was calculated and found to be 621 %/%RH. It was noted that the fabricated humidity sensor demonstrated an exceptionally high normalized sensitivity of approximately 621.3 per percent RH. The exceptionally high normalized impedance value is

View Article Online
DOI: 10.1039/D6NA00322B

characteristic of high-performance sensors, making it suitable for applications requiring the detection of minor variations in humidity.

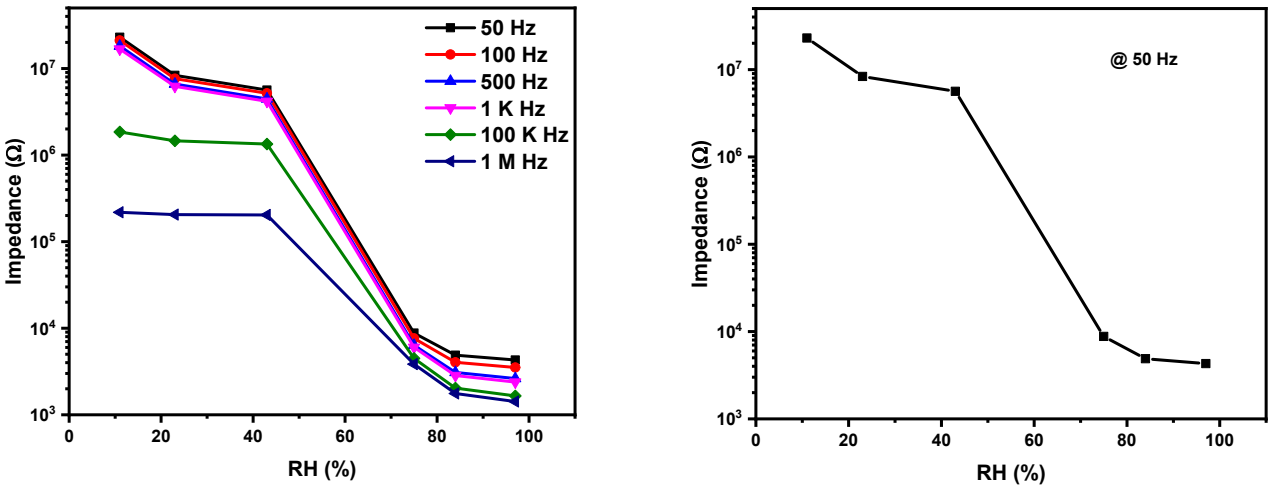

Fig.8: Humidity sensing response of the strontium iron vanadate ceramic sensor as a function of relative humidity at testing frequencies from 50 Hz to 5 MHz. (b) Impedance as a function of relative humidity at 50 Hz, showing the maximum total impedance change and the basis for the normalized sensitivity calculation.

The evaluation of humidity sensors is assisted by many factors, one of which is repeatability. The repeatability of the humidity sensor for multiple successive cycles at two different humidity levels is shown in **Fig. 9**. The repeatability tests were performed between 11% and 43%RH and 11% and 75%. The sensor was allowed to settle at each humidity level for 15 minutes. The evaluated sensor revealed a good repeatability with approximately no drift that reflects the excellent performance of the studied sensor. The response time is defined as the time taken by the sensor to attain 90% of its maximum value, while recovery time is defined as the time required by the sensor to return back to10 % of its original baseline value. The response and recovery times of the strontium iron vanadate were estimated from the repeatability curve and found to be 105 seconds and 245 seconds, respectively. The response and recovery times seem to be high; this could be related to

View Article Online
DOI: 10.1039/D6NA00322B

the moderate value of the negative zeta potential (-15 mV) that arises from surface hydroxylation of the perovskite oxide, where exposed metal-oxygen sites react with water to form hydroxyl (–OH) groups.

Table 2. Comparison of humidity sensing performance of the strontium iron vanadate ceramic sensor with selected metal oxide humidity sensors reported in the literature.

Sensing material	fabrication method	Sensing type	RH range (%, at RT)	Sensitivity	Response / recovery time	Reference
(Y, Sb)-co-doped TiO_2	Conventional ceramic route et al., 2024)	Capacitive	30 –95	165 and 386 pF/%RH	≈9 s / 7–4 s	[26]
Sr-doped $ZnFe_2O_4$ nanoparticles	Sol–gel	Resistive	10–95	1.918 MΩ/%RH for $Sr_{0.2}Zn_{0.8}Fe_2O_4$	19 s / 81 s	[27]
Sr-doped $LaFeO_3$ nanofibers	Electrospinning	Resistive	4–90	response factor 60579 at 90 % RH	N/A	[28]
$SrTiO_3$ nanospheres	Hydrothermal	Impedance	11–95	Impedance change of 4 orders of magnitude	2 s / 2 s	[29]
Sr-doped ZnO thin films	Sol–gel	Resistive	40–90	657.59x with Sr doping	0.8 s / 9.8 s	[30]
Porous SnO_2/TiO_2:Mo composite	Solid-state	Impedance	15–85	≈2 orders of magnitude change	18 s / 27 s	[31]
Fe-doped SnO_2 (Fe/SnO_2)	Hydrothermal	Resistive	11–95	Resistance increased from 4.5 to 5.5 orders vs pure SnO_2.	10 s / 8 s (vs 11 s / 48 s for undoped)	[32]
Sr_2FeVO_6	Sol-gel	Impedance	11-97	621 %/%RH	105 s /245 s	This work

View Article Online
DOI: 10.1039/D6NA00322B

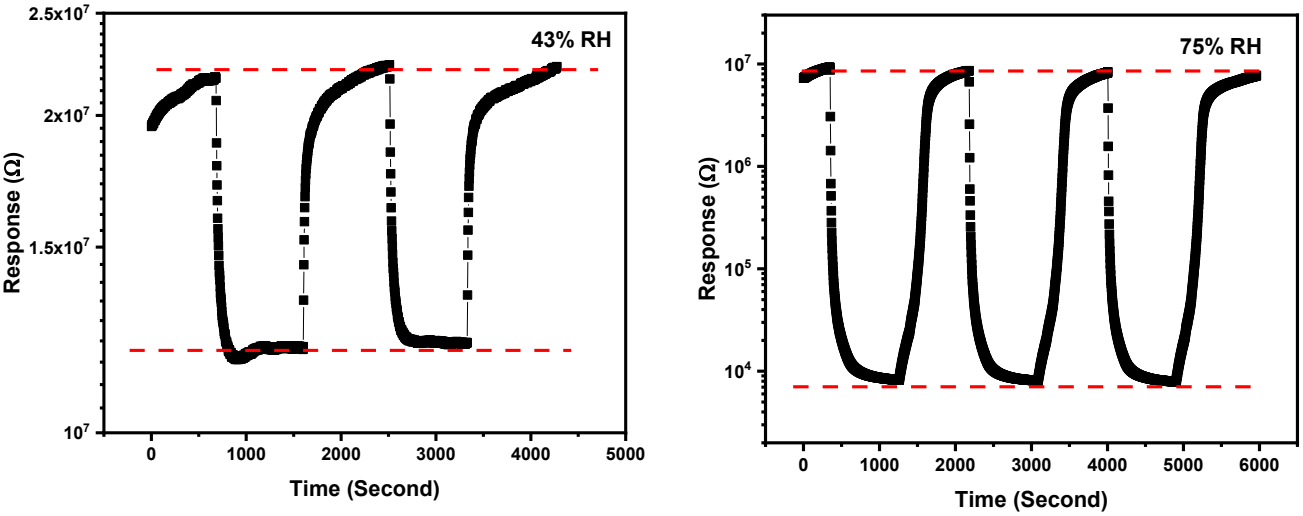

.

Fig. 9. Repeatability curves of the strontium iron vanadate ceramic humidity sensor measured between 11%–43% RH and 11%–75% RH over multiple successive cycles, showing stable response with no observable drift. Response and recovery times were estimated from these curves.

3.6.2 Impedance Spectroscopy Analysis

The frequency-dependent impedance response of the strontium iron vanadate ceramic humidity sensor was examined across 50 Hz to 5 MHz at RH levels from 11% to 97% RH, as presented in **Fig. 10** as plots of total impedance |Z|, phase angle θ, real component Z′, and imaginary component Z″. The total impedance |Z| decreases monotonically with increasing RH at all frequencies. At low RH levels (11%–43%), |Z| spans from approximately 10^7 Ω at low frequency to 10^4 Ω at high frequency, exhibiting strong frequency dispersion indicative of localized charge carrier hopping between surface hydroxyl sites and grain boundary regions, consistent with Maxwell-Wagner interfacial polarization at grain boundaries dominating the low-frequency response [17,26]. A sharp transition is observed between 43% and 75% RH, where |Z| drops by more than three orders of magnitude to the 10^3–10^4 Ω range and frequency dispersion

View Article Online
DOI: 10.1039/D6NA00322B

collapses substantially. At high RH (75%–97%), |Z| remains relatively flat across the frequency range, characteristic of long-range ionic conduction dominated by mobile hydronium ions. Notably, all RH curves converge toward similar |Z| values at the highest measured frequencies, reflecting the intrinsic lattice polarizability of strontium iron vanadate ceramic independent of moisture content. A sharp transition is observed between 43% and 75% RH, where |Z| drops by more than three orders of magnitude and frequency dispersion collapses substantially. The adsorbed water clusters are isolated at low RH%, but at a threshold (at 75% RH and above) the clusters connect forming a continuous conduction network, that activates bulk hydronium ion transport and replaces localized surface hopping as the dominant conduction mechanism.

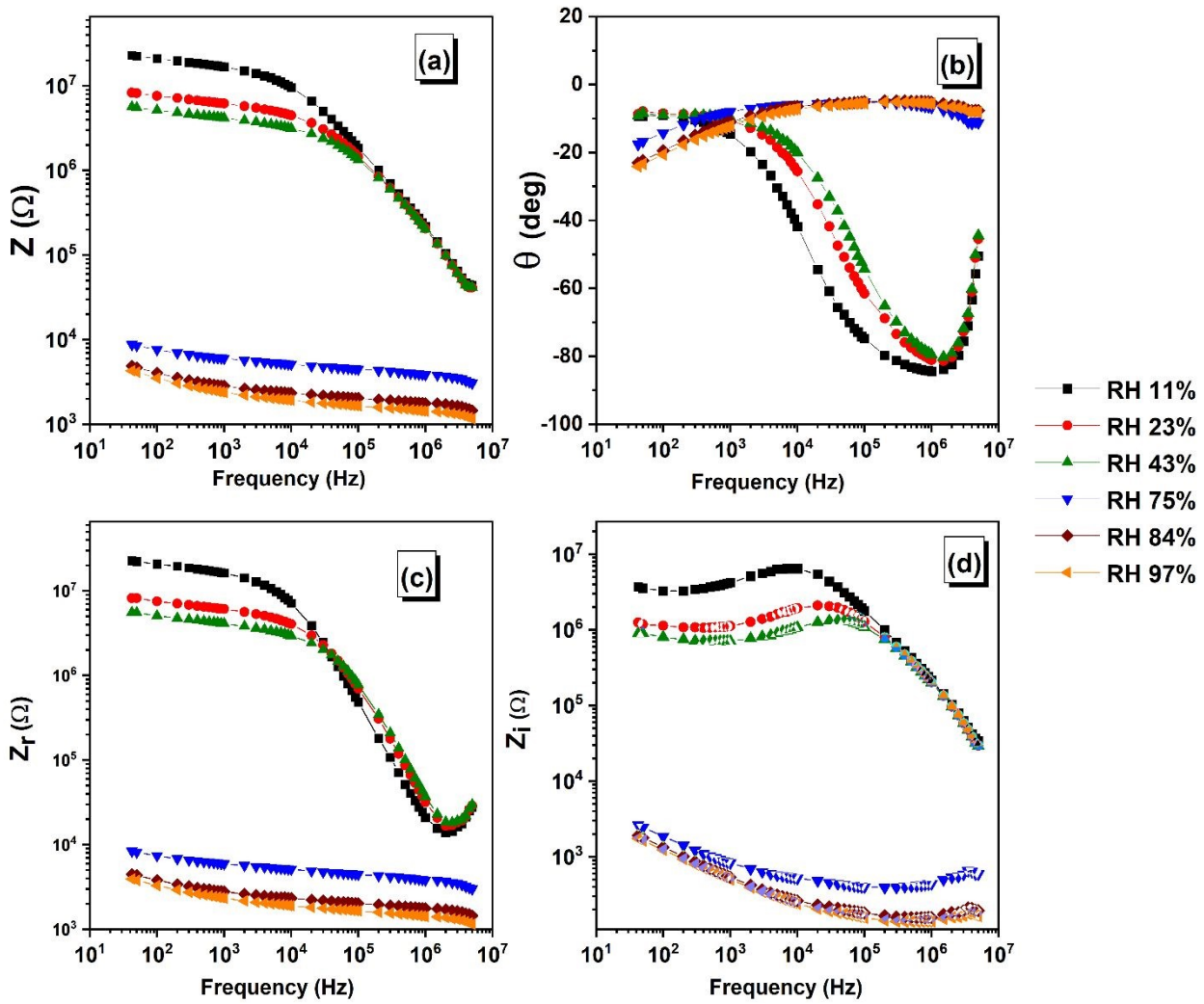

Fig. 10. Frequency-dependent impedance spectra (|Z|, θ, Z′, and Z″) of the strontium iron vanadate ceramic humidity sensor measured at 11%–97% RH.

View Article Online
DOI: 10.1039/D6NA00322B

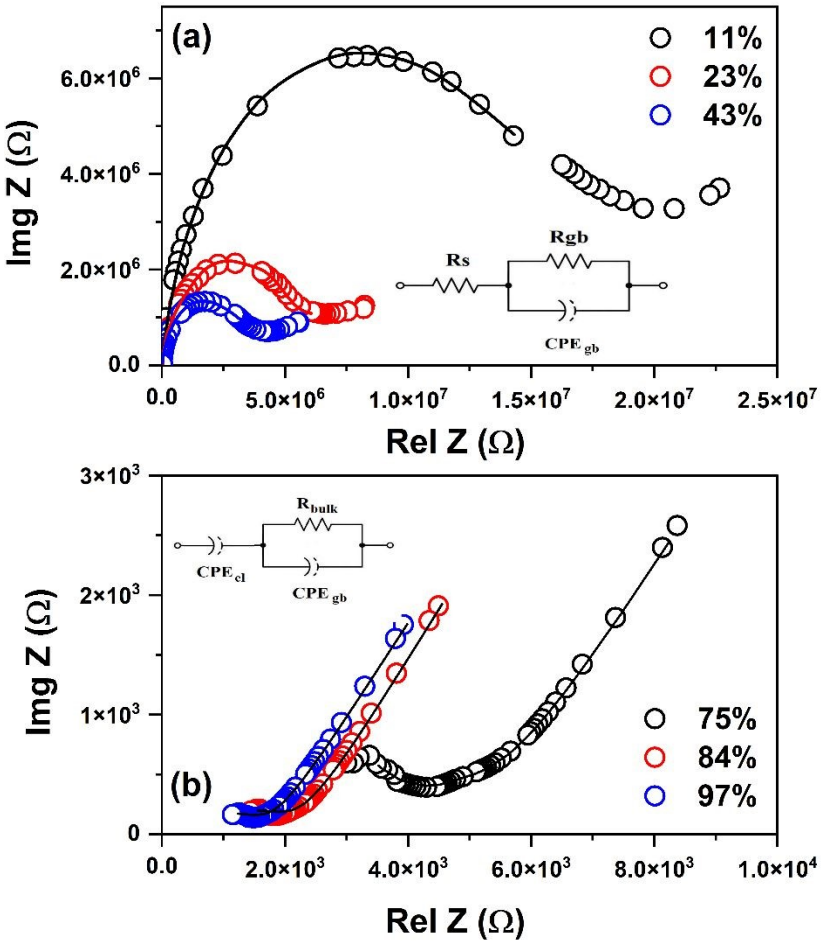

Fig. 11. Nyquist plots of the strontium iron vanadate ceramic humidity sensor at (a) 11%–43% RH fitted using Rs + [Rgb || CPEgb] over 1 kHz–1 MHz, and (b) 75%–97% RH fitted using CPE_{el} + [R_{bulk} || CPEgb]. Solid lines represent equivalent circuit fits. Circuit diagrams are shown as insets.

The phase angle θ is negative across the entire measured frequency and RH range, confirming the capacitive character of the sensor response throughout. At low RH (11%–43%), θ takes relatively small negative values at the lowest frequencies before deepening to a pronounced minimum of approximately −80° in the 10^5–10^6 Hz range, shifts to higher frequencies with increased RH level, reflecting strongly capacitive behavior associated with charge accumulation at grain boundaries and electrode interfaces in the absence of sufficient mobile charge carriers. The phase angle`s minimum perish at 75% RH and above, showing somewhat constancy at moderately negative small magnitudes, reflecting a move from strongly capacitive behavior to a weakly capacitive or predominantly resistive response. These changes are consistent with a

View Article Online
DOI: 10.1039/D6NA00322B

transition from localized, surface-bound conduction at low RH to bulk ionic transport at elevated humidity.

The real component Z′ transitions from strongly frequency-dispersive behavior at low RH to a frequency-independent plateau at 75% RH and above, characteristic of ohmic conduction driven by mobile hydronium ions. At high RH, Z′ transitions to a flat frequency-independent plateau characteristic of ohmic conduction, confirming that hydronium ions generated through the interaction of adsorbed water multilayers with surface hydroxyl groups act as the dominant charge carriers in this regime. The imaginary component Z″ exhibits a relaxation peak that shifts systematically to higher frequency with increasing RH, from approximately 8 kHz at 11% RH to 20 kHz at 23% RH and 40 kHz at 43% RH, corresponding to the characteristic relaxation frequency of the dominant polarization process at grain boundaries and surface adsorption sites.

This progressive shift reflects a systematic reduction in relaxation time as increasing water adsorption enhances charge carrier mobility even within the low-RH regime, prior to the percolation threshold. Above 75% RH the peak disappears entirely as the conduction mechanism transitions from localized hopping to long-range ionic transport and relaxation times extend beyond the measured frequency window.

The Nyquist plots in **Fig. 11** show well-defined semicircular arcs at low RH with diameters extending into the mega ohm range, consistent with the high impedance and capacitive character identified in the frequency-domain analysis. In this regime, charge carriers are localized at surface hydroxyl sites on the strontium iron vanadate ceramic grain surfaces, where the first monolayer of water is chemisorbed via hydrogen bonding. The first monolayer of water is chemisorbed via hydrogen bonding to surface hydroxyl groups on the strontium iron vanadate ceramic grain surfaces, with subsequent physisorbed layers forming at higher RH levels. As RH increases, the semicircle diameter contracts progressively by several orders of magnitude, driven by the generation of hydronium ions H_3O^+ through the reaction of physisorbed water molecules with the chemisorbed layer, producing mobile ionic charge carriers that facilitate proton hopping via the Grotthuss mechanism [33]. At 84% and 97% RH the semicircular arc collapses further as continuous water multilayers establish a percolating ionic conduction network through the sensor material. The progressive collapse of the semicircle diameter spanning more than four orders of

View Article Online
DOI: 10.1039/D6NA00322B

magnitude in impedance from 11% to 97% RH provides the mechanistic basis for the exceptional normalized sensitivity of 621 %/%RH observed at 50 Hz.

Collectively, the systematic evolution of |Z|, θ, Z′, Z″, and the Nyquist semicircle diameter with increasing RH is consistent with a percolation threshold at 75% RH, above which isolated adsorbed water clusters connect into a continuous conduction network and bulk ionic transport via the Grotthuss mechanism is activated.

Table 3. Equivalent circuit parameters fitted to the Nyquist data of the strontium iron vanadate ceramic humidity sensor at low relative humidity (11%–43% RH) using the circuit Rs + [Rgb // CPEgb] over 1 kHz–1 MHz.

Parameter	Symbol	RH 11%	RH 23%	RH 43%
Series Resistance	Rs(Ω)	37217	31817	20839
Grain Boundary Resistance	Rgb (Ω)	1.54×10^{7}	5.49×10^{6}	3.54×10^{6}
CPE Coefficient	P1 ($S\cdot s^{n}$)	2.57×10^{-12}	4.37×10^{-12}	4.21×10^{-12}
CPE Exponent	n1	0.919	0.891	0.895

Table 4. Equivalent circuit parameters fitted to the Nyquist data of the strontium iron vanadate ceramic humidity sensor at high relative humidity (75%–97% RH) using the circuit CPE_{el} + [R_{bulk} // CPEgb].

Parameter	Symbol	RH 75%	RH 84%	RH 97%
Bulk Ionic Resistance	R_{bulk}	5975.5	2503.7	1955.2
CPE_{el} Coefficient	P1 ($S\cdot s^{n}$)	2.11×10^{-5}	2.77×10^{-5}	3.20×10^{-5}
CPE_{e}l Exponent	n1	0.450	0.454	0.438
CPEgb Coefficient	P2 ($S\cdot s^{n}$)	4.58×10^{-6}	7.56×10^{-6}	6.51×10^{-6}
CPEgb Exponent	n2	0.195	0.203	0.223

The impedance spectra were analyzed using equivalent circuit fitting to extract quantitative parameters describing the humidity-dependent electrical response of the strontium iron vanadate ceramic sensor. Two circuits were applied, each corresponding to a distinct conduction regime identified from the impedance analysis.

At low relative humidity (11%–43% RH), the Nyquist plots show depressed semicircular arcs with diameters in the mega ohm range. The circuit Rs + [Rgb // CPEgb] was fitted over the 1 kHz–1 MHz frequency range, where the arc is well defined. Rs represents the high-frequency real-

View Article Online
DOI: 10.1039/D6NA00322B

axis intercept, combining contact resistance and unresolved grain interior resistance whose arc lies above the upper frequency limit of the measurement. Rgb is the grain boundary resistance and CPE is a constant phase element representing the distributed grain boundary capacitive response. The fitted parameters are presented in **Table 3**.

The fitting range was restricted to 1 kHz–1 MHz where the grain boundary arc is well defined. Below 1 kHz, the arc tail is incomplete and extends beyond the lower measurement limit, including this region introduces systematic misfit without physical justification. Above 1 MHz, the grain interior arc is unresolved and absorbed into Rs. The circuit Rs + [Rgb // CPEgb] is therefore applied only within the frequency range where it is physically valid.

Rs decreases from 37217 Ω at 11% RH to 20839 Ω at 43% RH, consistent with progressive mobilization of grain interior charge carriers through water adsorption prior to the percolation threshold. Rgb decreases from 1.54×10^{7} Ω at 11% RH to 3.54×10^{6} Ω at 43% RH, reflecting the reduction in grain boundary resistance with increasing surface water coverage. All Rgb values represent lower bounds, as the arc does not close within the measured frequency window. The CPE exponent n1 remains stable at approximately 0.90 across all three low RH levels, confirming consistently near-capacitive distributed grain boundary relaxation arising from the polycrystalline microstructure. At high relative humidity (75%–97% RH), the Nyquist response contracts to the kilo ohm range and the semicircular arc collapses. The circuit CPE_{el} + [R_{bulk} // CPEgb] was applied across the full measured frequency range. CPE_{el} represents electrode polarization arising from accumulation of mobile hydronium ions at the FTO electrode interface. R_{bulk} is the bulk ionic resistance reflecting long-range Grotthuss proton transport through the continuous water network established above the percolation threshold. CPEgb represents the residual grain boundary capacitive character retained above the percolation threshold. The necessity of CPEgb was confirmed by a substantial increase in reduced χ^2 upon its removal, establishing that it is not a decorative parameter. The fitted parameters are presented in **Table 4**.

R_{bulk} decreases monotonically from 5975 Ω at 75% RH to 1955 Ω at 97% RH, directly reflecting the growing population of mobile hydronium ions generated through the Grotthuss mechanism as water multilayers deepen with increasing RH. The CPE_{el} exponent n1 remains stable at approximately 0.45 across all three high RH levels, with a total variation of 0.016 within combined fitting error bounds. This stability confirms that the electrode polarization process has a

View Article Online
DOI: 10.1039/D6NA00322B

fixed distributed character determined by the FTO electrode geometry and surface roughness, independent of the humidity level. Only the CPE_{el} pre-factor P1 scales monotonically with RH, from 2.11×10^{-5} at 75% RH to 3.20×10^{-5} $S\cdot s^n$ at 97% RH, reflecting the growing accumulation of hydronium ions at the electrode interface with increasing water content. The CPEgb exponent n2 remains in the range 0.195–0.223 across 75%–97% RH, confirming that the grain boundary retains a near-resistive character above the percolation threshold, consistent with the dominance of bulk ionic transport over interfacial polarization in this regime.

The evolution of the equivalent circuit parameters across the full 11%–97% RH range provides quantitative confirmation of the two-stage sensing mechanism. The dominant resistance decreases continuously from 37217 Ω at 11% RH to 1955 Ω at 97% RH, spanning nearly one order of magnitude within the low RH regime alone and accelerating sharply above the percolation threshold. The CPE exponent transitions from $n \approx 0.90$ at low RH, reflecting near-ideal capacitive grain boundary behavior, to $n \approx 0.45$ at high RH, reflecting the near-Warburg distributed electrode polarization character of the ionic conduction regime. This systematic parameter evolution is fully consistent with the percolation threshold identified at 75% RH from the impedance, dielectric, and conductivity analysis presented in the preceding sections.

3.6.3 Dielectric and Conductivity analysis

The dielectric and conductivity properties of the strontium iron vanadate ceramic humidity sensor were examined as functions of frequency and relative humidity, and the results are presented in **Fig. 12** as plots of dielectric permittivity ε′, loss tangent tan δ, imaginary part of the electric modulus M″, and AC conductivity σ′.

View Article Online
DOI: 10.1039/D6NA00322B

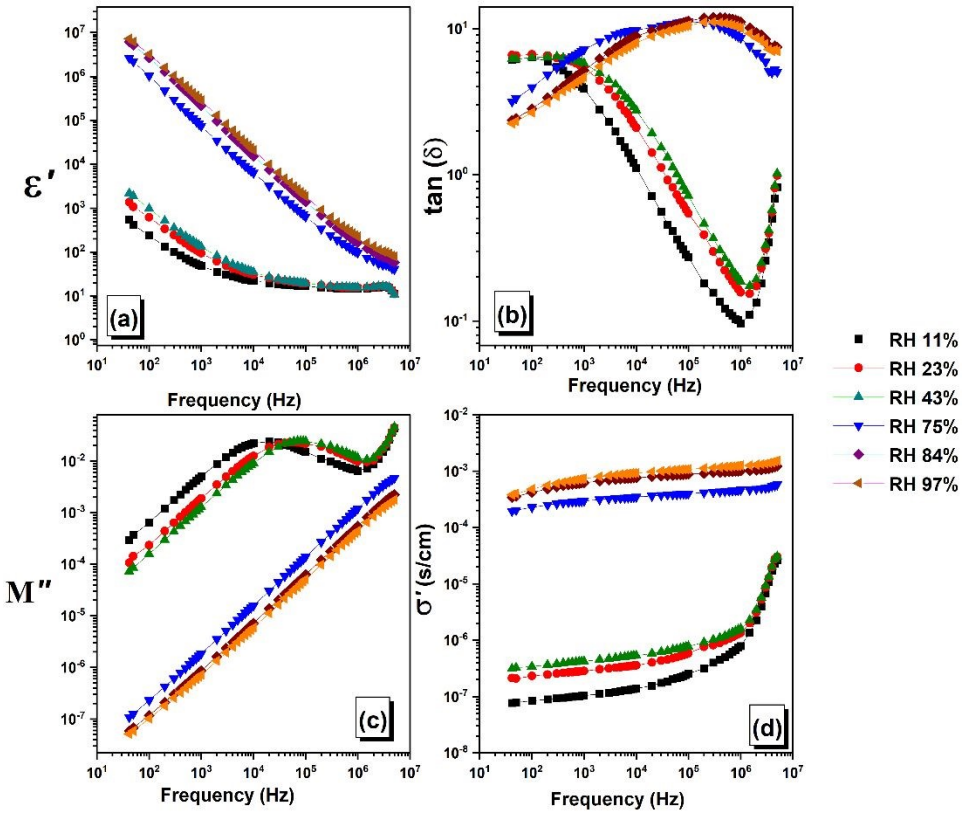

Fig. 12. Frequency-dependent dielectric permittivity (ε′), loss tangent (tan δ), electric modulus (M″), and AC conductivity (σ′) of the strontium iron vanadate ceramic humidity sensor at 11%–97% RH.

Dielectric Permittivity (ε′):

The dielectric permittivity ε′ decreases monotonically with increasing frequency at all RH levels. Two distinct behavioral groups are evident. At low RH (11%–43%), ε′ increases progressively within the group from approximately 10^2 at 11% RH to 10^3 at 43% RH at the lowest measured frequency — before decreasing steadily with a moderate dispersion slope, with all three curves converging to approximately 10–15 at high frequency. This progressive increase within the low RH group indicates that water adsorption enhances polarizability continuously even before the percolation threshold, while the high-frequency convergence reflects the intrinsic lattice polarizability of strontium iron vanadate ceramic, independent of surface water content. At 75% RH and above, ε′ reaches colossal values of 10^6–10^7 at low frequency and decreases steeply with a markedly stronger dispersion slope than the low RH group, reflecting the stronger frequency

View Article Online
DOI: 10.1039/D6NA00322B

dependence of space-charge polarization compared to intrinsic lattice response. Unlike the low RH group, where curves converge at high frequency, the high RH curves remain progressively separated from each other even at high frequency, indicating that water incorporation at and above the percolation threshold modifies the effective dielectric environment of the material beyond simple surface ionic conduction. The colossal low-frequency permittivity at high RH is consistent with Maxwell-Wagner interfacial polarization. Mobile hydronium ions generated via the Grotthuss mechanism [33] accumulate at grain boundaries and electrode interfaces under the applied AC field, producing giant space-charge polarization that dominates ε′ at low frequencies where ions have sufficient time to accumulate.

Dielectric loss tangent (tan δ):

The loss tangent tan δ shows markedly different behavior between the two RH regimes. At low RH (11%–43%), tan δ values converge toward each other at the lowest measured frequencies before decreasing to a well-defined minimum that shifts to higher frequency with increasing RH, then rising again at high frequency. The minimum represents a crossover between conduction-dominated loss at low frequency and relaxation-dominated loss at high frequency, while the subsequent high-frequency rise reflects the onset of relaxation losses as the applied frequency approaches the natural relaxation frequency of the dominant polarization process, consistent with the M″ relaxation peaks discussed below. At 75% RH and above, tan δ is consistently high — 5–10 — across most of the measured frequency range with no minimum visible, indicating that conduction loss dominates throughout as the high concentration of mobile hydronium ions produces continuous dissipation at all measured frequencies. At the highest measured frequencies, all RH curves converge toward similar tan δ values, paralleling the high-frequency ε′ convergence of the low RH group and reflecting the intrinsic high-frequency lattice response. The transition from a well-defined loss minimum at low RH to conduction-dominated loss at high RH is consistent with the percolation threshold identified from the impedance analysis.

Electric Modulus (M″):

The imaginary part of the electric modulus M″ is presented in preference to ε″, as the modulus formalism suppresses electrode polarization contributions and measurement artifacts

View Article Online
DOI: 10.1039/D6NA00322B

arising at high frequencies, providing a cleaner representation of bulk relaxation processes. At low RH (11%–43%), M″ shows well-defined relaxation peaks that shift systematically to higher frequency with increasing RH — from approximately 20 kHz at 11% RH to 50 kHz at 23% RH and 90 kHz at 43% RH — while maintaining approximately constant peak amplitude across the three RH levels. The systematic frequency shift with approximately constant amplitude indicates that increasing water adsorption reduces the relaxation time of charge carriers without significantly changing their number, consistent with progressive mobilization of existing surface-bound charge carriers rather than generation of new ones. This behavior is consistent with the Z″ relaxation peaks observed at 8, 20, and 40 kHz for the same RH levels in Section 3.X, and the M″ peaks appear at higher frequencies than the corresponding Z″ peaks, consistent with a distribution of relaxation times in the polycrystalline strontium iron vanadate ceramic microstructure arising from distinct grain boundary and grain interior contributions [19]. At 75% RH and above, no M″ peak is observed within the measured frequency window, with the curves showing a monotonic rise that approaches but does not reach a maximum within the measurement range, indicating that the characteristic relaxation frequency has shifted beyond the upper frequency limit of the measurement. This is consistent with long-range ionic conduction, where hydronium ions are fully mobile and relaxation times extend beyond the measurable window. The near-overlap of the 75%, 84%, and 97% RH curves in M″ — contrasting with their progressive separation in ε′ — reflects the suppression of electrode polarization contributions in the modulus formalism, confirming that M″ provides a cleaner view of the bulk relaxation response at high RH.

AC conductivity (σ′):

The AC conductivity σ′ increases with frequency at all RH levels but shows fundamentally different frequency dependence between the two conduction regimes. At low RH (11%–43%), σ′ increases progressively within the group — from approximately 10^{-7} S/cm at 11% RH to 10^{-6} S/cm at 43% RH at low frequency — and increases continuously with frequency following Jonscher's power law behavior [11], characteristic of localized hopping conduction at grain boundaries and surface hydroxyl sites, consistent with the relaxation behavior identified in the Z″ and M″ analysis. This progressive increase within the low RH group mirrors the systematic M″ and Z″ peak shifts and reinforces the narrative of continuous charge carrier mobilization before the percolation threshold. At 75% RH and above, σ′ increases by approximately four orders of

View Article Online
DOI: 10.1039/D6NA00322B

magnitude to 10^{-4}–10^{-3} S/cm, with the three high RH curves remaining progressively separated from each other, reflecting the continuing enhancement of ionic conductivity with increasing water content. A well-defined frequency-independent plateau characteristic of long-range DC ionic conduction is observed, extending to progressively higher frequencies with increasing RH as the growing population of mobile hydronium ions pushes the onset of dispersive AC conduction to higher frequencies. At 75% RH and above, a subtle deviation from the plateau is observed at the lowest measured frequencies, suggestive of incipient electrode polarization arising from partial accumulation of mobile ions at the FTO electrode interface, consistent with the establishment of long-range ionic transport above the percolation threshold. The four orders of magnitude increase in σ' from the dry state to 97% RH underlies the strong humidity sensing response of the fabricated sensor.

Collectively, the giant permittivity enhancement, conduction-dominated loss, shift of the M'' relaxation peak beyond the measurement window, and four orders of magnitude increase in σ' converge above the percolation threshold at 75% RH, confirming the transition from localized hopping to bulk ionic transport. This comprehensive mechanistic picture provides the basis for the exceptional normalized sensitivity of 621 %/%RH demonstrated by the strontium iron vanadate ceramic humidity sensor.

3.6.4 Humidity Sensing Mechanism

The comprehensive characterization data presented in the preceding sections converge on a coherent two-stage sensing mechanism that accounts for the humidity response of the strontium iron vanadate ceramic sensor across the full 11%–97% RH range.

At low relative humidity (11%–43%), water molecule adsorption is governed by the surface chemistry of the strontium iron vanadate ceramic grain surfaces. The negative zeta potential of −15 mV measured for strontium iron vanadate ceramic particles reflects surface hydroxylation of exposed metal-oxygen sites, consistent with moderate electrostatic affinity for dipolar water molecules. Surface hydroxyl groups identified by FTIR spectroscopy are consistent with serving as the primary adsorption sites, with the first water monolayer chemisorbed via hydrogen bonding to these groups. In this regime, charge carriers remain localized at grain

View Article Online
DOI: 10.1039/D6NA00322B

boundary and surface hydroxyl sites, as evidenced by the Jonscher power law behavior of σ′, the well-defined Z″ relaxation peaks, and the strongly capacitive phase angle response. The grain boundary dominated nature of this conduction is consistent with the offset between M″ and Z″ relaxation peaks, reflecting a distribution of relaxation times arising from distinct grain interior and grain boundary contributions in the polycrystalline microstructure [Macdonald ref].

The high density of grain boundary and interfacial sites available for charge carrier trapping in this regime is consistent with the hierarchical microstructure of strontium iron vanadate ceramic revealed by SEM and XRD — wherein micron-scale polyhedral grains of average size ~1.6 μm comprise aggregates of nanocrystallite domains of average size 51.4 nm, generating an abundant internal grain boundary density within each sensing grain. Even within the low RH regime, progressive water adsorption continuously mobilizes charge carriers — reflected in the systematic shifts of M″ and Z″ relaxation peaks to higher frequencies and the progressive increase in σ′ across 11%–43% RH — demonstrating that the sensing response is active and graded throughout the low humidity range, not only at the percolation threshold. The thick film SEM (Fig. 5) confirms that this granular morphology and inter-particle porosity are preserved after deposition on FTO, establishing that the microstructural features discussed here are representative of the actual sensing layer.

Between 43% and 75% RH, the sensing mechanism undergoes a distinct transition in conduction character, consistent with the establishment of a percolation threshold within this range. As water vapor pressure increases, physisorbed water multilayers develop above the chemisorbed monolayer, progressively filling the inter-particle pore network. The partially densified microstructure of the sol-gel derived strontium iron vanadate ceramic, with inter-particle porosity visible in SEM micrographs, is consistent with facilitated water vapor access to grain boundary regions throughout the sensing layer, enabling water network formation as the percolation threshold is approached. At 75% RH and above, isolated adsorbed water clusters connect into a continuous conduction network, activating bulk ionic transport and producing the sharp drop in |Z| observed in the impedance analysis. The inter-particle gaps observed in the thick-film SEM (Fig. 5) indicate that porosity is retained in the deposited sensing layer, consistent with the percolation behavior observed at 75% RH.

View Article Online
DOI: 10.1039/D6NA00322B

Above the percolation threshold (75%–97% RH), the sensing mechanism is dominated by Grotthuss proton transport through the continuous water network. Physisorbed water molecules interact with the chemisorbed hydroxyl layer on strontium iron vanadate ceramic grain surfaces, generating hydronium ions H_3O^+ that serve as mobile long-range charge carriers. Proton hopping through the hydrogen-bonded water network via the Grotthuss mechanism [ref] produces the frequency-independent σ′ plateau, the shift of the M″ relaxation peak beyond the measurement window, the colossal Maxwell-Wagner interfacial permittivity at low frequency, and the conduction-dominated tan δ response observed across most of the measured frequency range. The incipient electrode polarization signature in σ′ at the lowest measured frequencies is consistent with hydronium ions being sufficiently mobile to traverse the full sensor thickness and accumulate at the FTO electrode interface, providing supporting evidence for the establishment of long-range ionic transport above the percolation threshold. The progressive separation of the 75%, 84%, and 97% RH curves in both ε′ and σ′ reflects the continuing enhancement of the ionic charge carrier population and the deepening modification of the bulk dielectric environment with increasing water content, an effect consistent with water incorporation modifying the effective medium properties of the highly hydrated sensing layer beyond simple surface conduction. The secondary Sr-vanadate phases (MP1, $Sr_{10}V_6O_{25}$; MP2, Sr_2VO_4) identified by XRD are hydrophilic oxides with metal-oxygen surface terminations that facilitate surface hydroxylation under humid conditions. Their presence within the granular microstructure is consistent with the inter-particle porosity observed in the thick-film SEM (Fig. 5). These phases provide additional adsorption sites for water vapor. However, their minor phase fractions relative to the dominant perovskite matrix mean they act as microstructural modifiers that complement but do not govern the primary humidity sensing mechanism of Sr_2FeVO_6.

The two-stage mechanism, from chemisorption-controlled localized hopping at low RH to Grotthuss-dominated bulk ionic transport at high RH, is consistent with the structural features of strontium iron vanadate ceramic established by XRD and FTIR characterization. The perovskite-related framework with B-site ordering features, indicated by 20 superstructure reflections systematically absent in Pm-3m but permitted in Ia-3d, presents metal-oxygen surface sites that undergo hydroxylation, as confirmed by FTIR. The multi-phase microstructure with

View Article Online
DOI: 10.1039/D6NA00322B

nanocrystallite grain boundary density, inter-particle porosity, and hydrophilic surface chemistry collectively underpin the exceptional normalized sensitivity demonstrated by this sensor.

Conclusion

This study reports the sol-gel synthesis of strontium iron vanadate ceramic and its application as an impedance-type humidity sensor. The material comprised a perovskite-related framework with features related to Sr_2FeVO_6-type ordering (Ia-3d, 20 superstructure reflections systematically absent in Pm-3m) coexisting with Sr-vanadate phases. Structural characterization revealed a hierarchical microstructure: 51.4 nm crystallites, ~460 nm agglomerates, and ~1.6 μm grains, with inter-particle porosity and a hydrophilic surface (zeta potential −15 mV). FTIR confirmed metal-oxygen framework with BO_6 octahedral vibrations. Humidity sensing from 11 to 97% RH showed 621%/%RH normalized sensitivity at 50 Hz. Impedance analysis revealed two clearly separated conduction regimes: localized hopping mechanisms dominating at low relative humidity (RH) and long-range proton transport occurring through continuous water pathways at elevated RH. The results confirm a substantial enhancement in low-frequency dielectric permittivity (10^6–10^7), together with a conductivity increase of nearly four orders of magnitude and a transition toward conduction-dominated behavior at elevated humidity. The multi-phase architecture with abundant grain boundaries, porosity, and surface hydroxylation collectively enabled this performance. This work contributes to understanding metal-oxide humidity sensors with perovskite-related contributions.

Data Availability Statement

All the data generated or analyzed to support the findings of this study are available within the article.

Ethical Approval

Not applicable. This study does not contain any studies with human participants or animals performed by any of the authors.

View Article Online
DOI: 10.1039/D6NA00322B

Supplementary Information

Table S1. Complete XRD peak indexing for all 52 peaks identified in the 10–90° 2θ range

CRediT Author Statement

A.G. Darwish: Conceptualization, Visualization, Data curation, Methodology, Formal analysis, Software, writing – original draft, Writing – review & editing. **Mohamed I. Farouk:** Data curation, funding acquisition, formal analysis, writing—original draft, and writing – review & editing. **Mohamed Morsy:** methodology, conceptualization, data curation, formal analysis, writing – original draft, writing – review & editing.

Conflicts of interest

There are no conflicts of interest to declare

Acknowledgements

This work was supported and funded by the Deanship of Scientific Research at Imam Mohammad Ibn Saud Islamic University (IMSIU) (grant number IMSIU-DDRSP2602).

References

[1] P. V. Tuza, M.M.V.M. Souza, A Review of Synthesis, Characterization, Properties, and Applications of Double Perovskite Oxides, Inorganics 13 (2025) 372. https://doi.org/10.3390/inorganics13110372.

[2] S. Vasala, M. Karppinen, A2B′B″O6 perovskites: A review, Prog. Solid State Chem. 43 (2015) 1–36. https://doi.org/10.1016/j.progsolidstchem.2014.08.001.

[3] A.F.F. Alaih, D. Triyono, M.A. Dwiputra, F.A.A. Nugroho, Ultrafast and low-hysteresis humidity sensors based on mesoporous LaFe0.925Ti0.075O3 perovskite, Sensors Actuators B Chem. 412 (2024) 135810. https://doi.org/10.1016/J.SNB.2024.135810.

[4] K. Tambwe, N. Ross, P. Baker, T.-T. Bui, F. Goubard, Humidity Sensing Applications of

View Article Online
DOI: 10.1039/D6NA00322B

Lead-Free Halide Perovskite Nanomaterials, Materials (Basel). 15 (2022) 4146. https://doi.org/10.3390/ma15124146.

[5] D. Han, Y. Wang, J. Li, M. Gao, Y. Luan, M. Shao, N. Ma, Perovskite-Based Humidity Sensor, ACS Appl. Mater. Interfaces 18 (2026) 3360–3377. https://doi.org/10.1021/acsami.5c17730.

[6] X. Zhao, Y. Sun, S. Liu, G. Chen, P. Chen, J. Wang, W. Cao, C. Wang, Humidity Sensitivity Behavior of CH3NH3PbI3 Perovskite, Nanomaterials 12 (2022). https://doi.org/10.3390/nano12030523.

[7] R. Das, U. Chaudhuri, A. Chanda, R. Mahendiran, Broadband Electron Spin Resonance Study in a Sr 2 FeMoO 6 Double Perovskite, ACS Omega 5 (2020) 17611–17616. https://doi.org/10.1021/acsomega.0c02070.

[8] J. Valdés, D. Reséndiz, Á. Cuán, R. Nava, B. Aguilar, C.M. Cortés-Romero, O. Navarro, Sol-Gel Synthesis of the Double Perovskite Sr2FeMoO6 by Microwave Technique, Materials (Basel). 14 (2021) 3876. https://doi.org/10.3390/ma14143876.

[9] Z. Wang, Q. Tang, Z. Wu, K. Yi, J. Gu, X. Zhu, B-Site Fe/Re Cation-Ordering Control and Its Influence on the Magnetic Properties of Sr2FeReO6 Oxide Powders, Nanomaterials 12 (2022) 3640. https://doi.org/10.3390/nano12203640.

[10] R. Masrour, G. Kadim, A. Jabar, E.K. Hlil, M. Ellouze, Emerging opportunities for Sr2FeReO6 and Sr2CrWO6 double perovskites in potential magnetic refrigerants and spintronics in room temperature regime, Appl. Phys. A 128 (2022) 1023. https://doi.org/10.1007/s00339-022-06152-1.

[11] A. Darwish, M.I. Farouk, M. Morsy, A. Elzwawy, ZnCo (2− x) Ce x O 4 , (x =0–1.0 wt%): optimized structural, morphological, dielectric, and magnetic properties for humidity sensing applications, Nanoscale Adv. 7 (2025) 5166–5183. https://doi.org/10.1039/D5NA00355E.

[12] T. Xie, A.F. Abdul Rahman, A. Abu Bakar, A. Arsad, Design and Optimization of Metal Oxide-Based Humidity Sensors: A Review on Mechanisms and Material Engineering, J. Clust. Sci. 36 (2025) 148. https://doi.org/10.1007/s10876-025-02869-0.

[13] H. Chen, A. Millis, Design of new Mott multiferroics via complete charge transfer:

View Article Online
DOI: 10.1039/D6NA00322B

promising candidates for bulk photovoltaics, Sci. Rep. 7 (2017) 6142. https://doi.org/10.1038/s41598-017-06396-5.

[14] Z. Pei, X. Zhou, K. Leng, W. Xia, Y. Wei, X. Zhu, Structural characterizations and dielectric, magnetic, and optical properties of Ba2FeVO6 double perovskite ceramics, AIP Adv. 10 (2020). https://doi.org/10.1063/5.0011677.

[15] J. Sahu, B.N. Parida, N.C. Nayak, R. Padhee, S.K. Parida, Studies of structure, microstructure, dielectric, and electrical properties of Mg2FeVO6 ceramic for device application, J. Electroceramics (2025). https://doi.org/10.1007/s10832-025-00439-4.

[16] G.M.G. da Silva, P.M. Faia, S.R. Mendes, E.S. Araújo, A Review of Impedance Spectroscopy Technique: Applications, Modelling, and Case Study of Relative Humidity Sensors Development, Appl. Sci. 14 (2024) 5754. https://doi.org/10.3390/app14135754.

[17] N. Thanamoon, N. Thongyong, K. Sreejivungsa, N. Chanlek, P. Thongbai, Enhanced humidity-sensing performance of (Zr 4+ /Sb 5+)-codoped TiO 2 ceramics with giant dielectric properties, J. Adv. Ceram. 14 (2025) 9221005. https://doi.org/10.26599/JAC.2024.9221005.

[18] Z. Chen, C. Lu, Humidity Sensors: A Review of Materials and Mechanisms, Sens. Lett. 3 (2005) 274–295. https://doi.org/10.1166/sl.2005.045.

[19] I.M. Hodge, M.D. Ingram, A.R. West, Impedance and modulus spectroscopy of polycrystalline solid electrolytes, J. Electroanal. Chem. Interfacial Electrochem. 74 (1976) 125–143. https://doi.org/10.1016/S0022-0728(76)80229-X.

[20] I.M. Hodge, M.D. Ingram, A.R. West, A new method for analysing the a.c. behaviour of polycrystalline solid electrolytes, J. Electroanal. Chem. Interfacial Electrochem. 58 (1975) 429–432. https://doi.org/10.1016/S0022-0728(75)80102-1.

[21] C.J. Bartel, C. Sutton, B.R. Goldsmith, R. Ouyang, C.B. Musgrave, L.M. Ghiringhelli, M. Scheffler, New tolerance factor to predict the stability of perovskite oxides and halides, Sci. Adv. 5 (2019). https://doi.org/10.1126/sciadv.aav0693.

[22] A.A. Bhran, R.M. Sabry, M.A. Farag, A.G. Gadallah, A.G. Darwish, Multifunctional evaluation of dielectric, optical, magnetic, and methylene blue adsorption behaviors of Ba2FeVO6 double perovskite, J. Mater. Sci. Mater. Electron. 36 (2025) 2056.

View Article Online
DOI: 10.1039/D6NA00322B

https://doi.org/10.1007/s10854-025-16088-w.

[23] D.N. Singh, M.K. Shamim, G. Panchal, R.J. Choudhary, A.K. Yadav, S.N. Jha, D. Bhattacharyya, A. Molak, D.K. Mahato, Probing the effect of Zn2+ on the local structure, dielectric and magnetic properties of La2CuMnO6 by solid state synthesis, J. Alloys Compd. 936 (2023) 168241. https://doi.org/10.1016/j.jallcom.2022.168241.

[24] A.M. Bakr, M. Morsy, A.M. El Nahrawy, A.B. Abou Hammad, Impact of reduced graphene oxide on spectroscopic properties of high-κ dielectric ZnTiO3 nanostructure for humidity sensing capabilities, Inorg. Chem. Commun. 174 (2025) 113955. https://doi.org/10.1016/j.inoche.2025.113955.

[25] E.S. Kim, J.S. Jeon, K.H. Yoon, Effect of sintering method on the microwave dielectric properties of (Pb0.45Ca0.55)(Fe0.5Nb0.5)O3 ceramics, J. Eur. Ceram. Soc. 23 (2003) 2583–2587. https://doi.org/10.1016/S0955-2219(03)00176-6.

[26] N. Thanamoon, N. Thongyong, K. Sreejivungsa, N. Chanlek, W. Jarernboon, P. Thongbai, Outstanding dielectric permittivity and humidity sensitivity in (Y/Sb) co doped TiO2 ceramics with rapid response/recovery time, Sensors Actuators B Chem. 419 (2024) 136372. https://doi.org/10.1016/j.snb.2024.136372.

[27] P.R. Tiwari, R.P. Singh, K. Bharati, A.C. Yadav, B. Bhardwaj, B.C. Yadav, A. Singh, S. Kumar, Synthesis and application of strontium-doped zinc ferrite nanomaterial in humidity sensing, J. Indian Chem. Soc. 101 (2024) 101439. https://doi.org/10.1016/j.jics.2024.101439.

[28] Z. Zhang, F. Li, Y. Zheng, Highly sensitive resistive humidity sensor based on strontium-doped lanthanum ferrite nanofibers, Sensors Actuators A Phys. 358 (2023) 114435. https://doi.org/10.1016/j.sna.2023.114435.

[29] D. Li, J. Zhang, L. Shen, W. Dong, C. Feng, C. Liu, S. Ruan, Humidity sensing properties of SrTiO 3 nanospheres with high sensitivity and rapid response, RSC Adv. 5 (2015) 22879–22883. https://doi.org/10.1039/C5RA00451A.

[30] G. Algün, N. Akçay, H.O. Öztel, M.M. Can, Synthesis and ultrafast humidity sensing performance of Sr doped ZnO nanostructured thin films: the effect of Sr concentration, J. Sol-Gel Sci. Technol. 107 (2023) 640–658. https://doi.org/10.1007/s10971-023-06148-0.

View Article Online
DOI: 10.1039/D6NA00322B

[31] D.L. Sekulić, T.B. Ivetić, Characterization of an Impedance-Type Humidity Sensor Based on Porous SnO2/TiO2 Composite Ceramics Modified with Molybdenum and Zinc, Sensors 23 (2023) 8261. https://doi.org/10.3390/s23198261.

[32] H. Zhang, H. Zhang, J. Man, C. Chen, Preparation of high performance Fe-doped SnO2 humidity sensor and its application in respiration detection, Sensors Actuators A Phys. 362 (2023) 114644. https://doi.org/10.1016/j.sna.2023.114644.

[33] I. Popov, Z. Zhu, A.R. Young-Gonzales, R.L. Sacci, E. Mamontov, C. Gainaru, S.J. Paddison, A.P. Sokolov, Search for a Grotthuss mechanism through the observation of proton transfer, Commun. Chem. 6 (2023) 77. https://doi.org/10.1038/s42004-023-00878-6.

View Article Online
DOI: 10.1039/D6NA00322B

Data Availability Statement

All the data generated or analyzed to support the findings of this study are available within the article.